https://doi.org/10.5194/jecats-2026-16
Preprint. Discussion started: 25 August 2026

A new ice crystal formation pathway in contrails generated by fuel cell propelled aircraft

Dennis Hillenbrand[1,2] and Simon Unterstrasser[1]

[1]Deutsches Zentrum für Luft- und Raumfahrt, Institut für Physik der Atmosphäre, Oberpfaffenhofen, Germany
[2]Delft University of Technology, Aerospace Engineering, Section Aircraft Noise and Climate Effects, Delft, the Netherlands

Correspondence: Dennis Hillenbrand (dennis.hillenbrand@dlr.de)

Abstract. We analyze ice crystal formation behind future hydrogen fuel cell-propelled aircraft via simulations using the particle-based Lagrangian Cloud Module (LCM) in a box model approach. Unlike conventional kerosene combustion, the exhaust of these aircraft could be significantly more humid and contain no soot particles, resulting in larger supersaturation values during plume cooling. These conditions can promote water droplet formation via Homogeneous Droplet Nucleation (HDN), which may substantially increase the number of contrail ice crystals. We implement the HDN into the LCM box model and validate the implementation against benchmark cases from the International Wet Steam Modeling Project. For the first time, the impact of HDN on ice crystal number in nascent contrails is quantified for exhaust parameters representative of fuel cell-propelled aircraft. We demonstrate that a low exhaust temperature together with high exhaust humidity leads to a large increase in ice crystal numbers due to additional droplet formation via HDN and their subsequent freezing. This would amplify the climate-forcing potential of an individual contrail. Conversely, reducing water vapour emissions suppresses HDN and effectively reduces the ice crystal number. The increase in ice crystal numbers is higher in cold ambient conditions $T_{\mathrm{amb}} \lessapprox 218\mathrm{K}$, which are, however, not expected to occur often on low flight levels of propeller aircraft. A sensitivity analysis reveals that faster plume dilution can lead to an increase of ice crystal number by orders of magnitude through an increased HDN rate. We propose that the slope G of the mixing line, which describes the thermodynamical conditions of the diluting plume, should be kept below around $G < 10\,\mathrm{Pa\,K^{-1}}$ by technical means to ensure that HDN does not occur, regardless of the ambient conditions.

1 Introduction

1.1 Motivation

Approximately $3.5\,\%$ of global anthropogenic effective radiative forcing (ERF) is attributed to the aviation industry (Lee et al., 2021). Additionally, projections indicate that air traffic will grow with an average annual rate between $2.6\,\%$ and $5.6\,\%$ depending on the region, from 2023 to 2043 (Aviation Benefits, 2024). Most of the currently delivered aircraft run on conventional gas turbines fueled by kerosene or sustainable aviation fuels (SAF) blends. While future turbo-fan aircraft will emit substantially less CO_2 compared to the current generation, this is not sufficient to meet the ambitious reduction targets for the aviation industry set by the European Commission (see Fig. 1 in Fuel Cells and Hydrogen 2 Joint Undertaking (2020)). Their Flightpath-2050

https://doi.org/10.5194/jecats-2026-16
Preprint. Discussion started: 25 August 2026

Table 1. Combustion heat Q (Ansell, 2023) and emission index of water vapour $\mathrm{EI_{H_2O}}$ for various fuels.

fuel	Kerosene	Hydrogen	Ammonia	LNG
$Q\,/\,\mathrm{MJ\,kg^{-1}}$	43	120	18.6	53.6
$\mathrm{EI_{H_2O}}\,/\,\mathrm{kg\,kg^{-1}}$	1.25	8.94	1.59	2.25

strategy aims to reduce CO_2 and NO_x emissions by $75\,\%$ and $90\,\%$, respectively (Commission et al., 2011). Achieving these targets in the face of projected air traffic growth presents a substantial challenge, but is essential nonetheless.

Less than half of the aviation sector's total effective radiative forcing may be attributed to CO_2 emissions with the remainder attributed to non-CO_2 effects, including NO_x emissions and contrail-cirrus formation (Lee et al., 2021). Among these, contrail-cirrus represent the largest contribution to aviation's radiative forcing, as illustrated in Fig. 1 of Lee et al. (2023). The radiative impact of contrail-cirrus is highly sensitive to both emission characteristics of the aircraft and local atmospheric conditions. These atmospheric conditions vary significantly in space and time due to weather variability (Wilhelm et al., 2021). Consequently, assessing the contrail-cirrus ERF is more complex than that of CO_2, which can be estimated via cumulative emission inventories. While current environmental objectives for future aircraft technologies emphasize reductions in CO_2 and NO_x emissions, there is a critical need to ensure that such advancements do not increase the radiative forcing associated with contrail-cirrus. This could occur if future propulsion systems lead to more frequent contrail formation, enhanced persistence, or increased optical thickness of contrail-cirrus.

1.2 Contrail formation

Contrails form if an aircraft plume becomes supersaturated with respect to water during its mixing with the ambient air and formed droplets freeze into ice crystals. A formed contrail remains liquid, if the ambient temperature $T_{\mathrm{amb}} > T_{\mathrm{frz}}$ is larger than the homogeneous freezing temperature of super-cooled water. These liquid contrails quickly dissolve as the ambient air is not supersaturated with respect to water.

A straightforward method to determine whether a contrail forms behind an aircraft is the well-known Schmidt–Appleman criterion (SAC) (Schumann, 1996). With this purely thermodynamic criterion the limiting ambient temperature T_{lim}, below which a contrail forms, can be calculated. Typically, T_{lim} is around $225\,\mathrm{K}$ to $230\,\mathrm{K}$ for conventional kerosene combustion. T_{lim} varies with both the overall propulsion efficiency and the fuel type utilized by the aircraft. Several studies have explored SAC formulation tailored to specific aircraft propulsion technologies. For instance, Gierens (2021) developed a framework for aircraft propelled by fuel cells (FCs), whereas Yin et al. (2020) expanded the SAC concept to include hybrid-electric propulsion architectures. More recently, Richardson (2025) conducted an assessment of contrail formation across a wide range of propulsion technologies. While the classical SAC is based on several linearizations that are no longer justifiable for very moist exhaust, (Hillenbrand and Unterstrasser, 2026) demonstrate the classical SAC remains valid as it turns out that physically unrelated linearization errors cancel each other.

https://doi.org/10.5194/jecats-2026-16
Preprint. Discussion started: 25 August 2026

For fuels like pure hydrogen or ammonia, the energy-specific water vapour (WV) emission increases compared to kerosene (see Table 1), leading to higher T_{lim} values. Therefore, using pure hydrogen as aviation fuel, contrail formation is possible at lower flight altitudes (Hofer et al., 2024), associated with higher ambient temperatures. An increase in potential contrail formation regions compared to conventional kerosene propelled engines has been shown for both hydrogen combustion (Dischl et al., 2024) and hydrogen based fuel cells (Kaufmann et al., 2024).

For kerosene and SAF combustion, the number of ice crystals is mainly governed by the soot emissions when the emission index of soot $\mathrm{EI_{soot}} \gtrapprox 10^{15}(\mathrm{kg\,fuel})^{-1}$ (Kleine et al., 2018; Voigt et al., 2021; Märkl et al., 2024). In the very low soot regime (i.e. engines with lean burn combustors), the volatile particles, resulting either from sulfur in the fuel or organic emissions (unburned hydrocarbons, lubrication oil), play a major role. There is also an "intermediate $\mathrm{EI_{soot}}$" region where both soot and volatile particles can contribute to the total number of ice crystals (Dischl et al., 2024; Voigt et al., 2026). For the case of hydrogen combustion, it can either be governed by ambient aerosol or lubrication oil activation, depending on the number of emitted oil droplets (Zink et al., 2025b). (Hillenbrand and Unterstrasser, 2026) showed that low exhaust temperature and high WV emissions from hydrogen-based FC-propelled (H_2FC) aircraft can lead to relative humidity values well above $\mathrm{RH_{w,plume}} > 500\,\%$ during the cooling of the aircraft plume. Such highly supersaturated conditions in the plume can trigger an additional microphysical process, where water droplets form without the need of condensation nuclei. This process is called Homogeneous Droplet Nucleation (HDN) and is known to occur e.g. in gas turbines for steam applications (Wittmann et al., 2021; Starzmann et al., 2018). HDN can lead to the formation of very many small water droplets. In the case of contrails, these can freeze into ice crystals in sufficiently cold environments.

The number of ice crystals formed during the initial formation phase influences the radiative effect of an individual contrail (Unterstrasser and Gierens, 2010; Lottermoser and Unterstrasser, 2026). An increase in the initial ice crystal number is associated with an increase in the contrail's radiative forcing (Burkhardt et al., 2018). Due to the lack of emitted particles, ice formation for H_2FC aircraft is limited to either heterogeneous nucleation on ambient aerosols or homogeneous nucleation via HDN.

1.3 Fuel Cell technology

A fuel cell is an electrochemical cell that converts the chemical potential of the utilized fuel via a pair of red-ox reactions into electrical energy. The key advantage of employing FC technology in aviation is that neither NO_x nor CO_2 are emitted, since propulsion is achieved through electrochemical processes rather than combustion. Propulsion based on pure hydrogen usage will, however, lead to H_2 leakages (either directly during cruise or indirectly on the ground from the H_2 infrastructure, increasing H_2 emissions into the atmosphere (Adler and Martins, 2023; Ocko and Hamburg, 2022). Apart from these leakages, FC propulsion systems only emit water (vapour), air and heat. This means that the radiative forcing of future H_2FC aircraft will be dominated by its contrail effect.

The technical realization of H_2FC aircraft presents a number of challenges, including the storage of liquefied hydrogen and the necessity to increase the power density of FC units, which will lead to a later expected entry-into-service of hydrogen based H_2FC aircraft compared to hydrogen combustion in the aviation sector (Baroutaji et al., 2019). Furthermore, a large

https://doi.org/10.5194/jecats-2026-16
Preprint. Discussion started: 25 August 2026

amount of the available electrochemical energy (approximately 50 %) is converted into heat within the fuel cell, necessitating the use of efficient heat exchangers to maintain a constant operating temperature for the FC stacks. This results in increased complexity and weight for the FC propulsion system, further limiting the gravimetric power density of FC propulsion (Kazula et al., 2023). Therefore, it is expected that H_2FC aircraft will mainly be introduced for the regional sector. Nevertheless, the first H_2FC aircraft with four passenger seats from HY4, demonstrated the general feasibility of this future technology in the aviation sector (HY4, 2016).

At present, the most promising options for integrating fuel cells into commercial aircraft are expected to be PEM-FC (proton exchange membrane fuel cell) and SO-FC (solid oxide fuel cell) (Kazula et al., 2023). PEM-FC are sub-categorized into low temperature (LT) PEM-FCs, that operate approximately at $80-100$ °C, and high temperature (HT) PEM-FC, whose operating temperature reaches up to 200 °C (Frey et al., 2025). PEM-FC systems achieve the highest technology readiness level compared to other types of FC systems (Kazula et al., 2023). Nevertheless, these systems need complex water management for the humidification of the electrolytes and efficient heat management to ensure the low operating temperature. The higher operating temperature of SO-FC systems reduces the requirements for heat management, yet it increases thermal stress of the components. While SO-FC systems are expected to have higher efficiencies, further research is necessary for those FC types (Kazula et al., 2023).

Regardless of the particular FC setup, the gas leaving the FC stack can be modified by additional systems (Hillenbrand and Unterstrasser, 2026). Possible options are additional heat exchangers to use parts of the otherwise unused thermal energy of the gas within the aircraft, or water condenser systems to reduce the WV amount in the gas. The possibilities and options of a technical realization of FC technology in aviation are manifold and subject to current and future research. This leads to a large variety of hypothetical exhaust properties of H_2FC aircraft, which has a significant impact on the contrail formation stage. It is expected that low exhaust temperature values increase both the contrail formation propensity and peak supersaturation values during plume cooling for H_2FC aircraft.

The purpose of this study is to describe how the LCM box model has been extended to capture HDN and to explore its relevance in contrail formation behind H_2FC aircraft. Section 2 summarizes the numerical setup used and the LCM box model framework. Section 3 is dedicated to HDN and describes its implementation in the LCM box model, numerical convergence test and the validation by comparison with reference benchmark test cases. Section 4 explores the relevance of HDN for a large range of possible H_2FC exhaust properties and meteorological conditions. We conclude with a discussion (Sec. 5) and conclusion (Sec. 6).

2 Numerical methods and model setup

2.1 Exhaust properties of H_2FC aircraft

In H_2FC aircraft, active thermal management via heat exchangers is essential to maintain a stable operating temperature within the FC stack (Kazula et al., 2023). These heat exchangers not only enable effective thermal regulation but also offer the potential for waste heat recovery, thereby enhancing the overall propulsion efficiency and reducing exhaust gas temperatures.

https://doi.org/10.5194/jecats-2026-16
Preprint. Discussion started: 25 August 2026

Analogously, Hillenbrand and Unterstrasser (2026) proposed the integration of water vapour condensers to mitigate high moisture contents in the exhaust stream. To quantify the effect of these recuperative strategies, two relative emission factors have been introduced in Hillenbrand and Unterstrasser (2026):

- $\gamma = \mathrm{EI}_{\mathrm{H_2O,emit}}/\mathrm{EI}_{\mathrm{H_2O}}$ is the ratio of emitted to unaltered WV amount
- $\delta = Q_{\mathrm{emit}}/Q_{\mathrm{avail}}$ is the ratio of emitted to unaltered heat

In this framework, $\gamma = \delta = 1$ correspond to no reduction, whereas γ or $\delta = 0.4$ represent a $60\,\%$ reduction of the theoretical emission value. Fig. 1 shows a schematic representation of contrail-relevant components for a hypothetical FC-based propulsion concept, as introduced in Hillenbrand and Unterstrasser (2026), including the relative emission factors γ and δ. The heat exchangers extract thermal energy from the FC stack, which can either be utilized within the aircraft systems, released in a separate 'dry-air' exhaust stream (labelled '2' in Fig. 1) or mixed with the 'moist-air' exhaust stream (labelled '1' in the sketch). Consequently, the exhaust contains only a fraction of the energy that is not used to propel the aircraft. The thermal energy released in the contrail forming exhaust can be expressed as $\delta\, Q\, (1-\eta)$ with the combustion heat Q of the fuel, and the overall propulsion efficiency η.

To reduce the WV amount in the 'moist-air' exhaust stream ('1'), a WV condenser could be included into the aircraft. Ensuring that the condensed water is emitted in a separate exhaust stream ('3' in Fig. 1), such that it cannot re-moisturize the other exhaust streams, this reduces the humidity within the contrail forming exhaust to $\gamma\, \mathrm{EI}_{\mathrm{H_2O}}$, where $\mathrm{EI}_{\mathrm{H_2O}}$ is the emission index of water vapour of the fuel.

The thermodynamic exhaust properties also depend on the initial air-to-fuel ratio $\mathcal{C}_{\mathrm{E}}$, representing the ratio of fuel mass to the mass of ambient air at the time of emission. With the relative emission factors γ, δ and $\mathcal{C}_{\mathrm{E}}$, the exhaust temperature T_{E} and specific humidity q_{E} can be calculated by

$$q_{\mathrm{E}} = q_{\mathrm{a}} + \gamma \frac{\mathrm{EI}_{\mathrm{H_2O}}}{\mathcal{C}_{\mathrm{E}}} \quad (1)$$

$$T_{\mathrm{E}} = T_{\mathrm{a}} + \delta \frac{Q(1-\eta)}{c_p \mathcal{C}_{\mathrm{E}}} \quad (2)$$

where c_{p} is the specific heat capacity of dry air, which is assumed to be constant $c_{\mathrm{p}}(q,T) \approx c_{\mathrm{p}} = 1004\,\mathrm{J\,(kg\,K)^{-1}}$ and the subscripts 'E' and 'a' denote exhaust and ambient conditions, respectively.

Taking γ and δ into account, Hillenbrand and Unterstrasser (2026) extended the definition of the SAC mixing line, as introduced in the seminal paper of Schumann (1996), to

$$p_{\mathrm{wv}}(T) = p_{\mathrm{wv,a}} + G_{\mathrm{FC}}(T - T_{\mathrm{a}}) \text{ with} \quad (3)$$

$$G_{\mathrm{FC}} = \frac{\gamma\, \mathrm{EI}_{\mathrm{H_2O}}\, c_{\mathrm{p}}\, p_{\mathrm{a}}}{\delta\, Q\, (1-\eta)\, \epsilon}, \quad (4)$$

where p_{a} denotes the ambient pressure and ϵ is the ratio of the molar masses of water and dry air $\epsilon = M_{\mathrm{H_2O}}/M_{\mathrm{da}} \approx 0.622$. Deviations of γ and δ from 1 change the exhaust temperature and moisture, which also results in implicit changes of other exhaust properties. The exhaust mass flow rate $\dot{m}_{\mathrm{E}}$ can be derived from the ideal gas law:

https://doi.org/10.5194/jecats-2026-16
Preprint. Discussion started: 25 August 2026

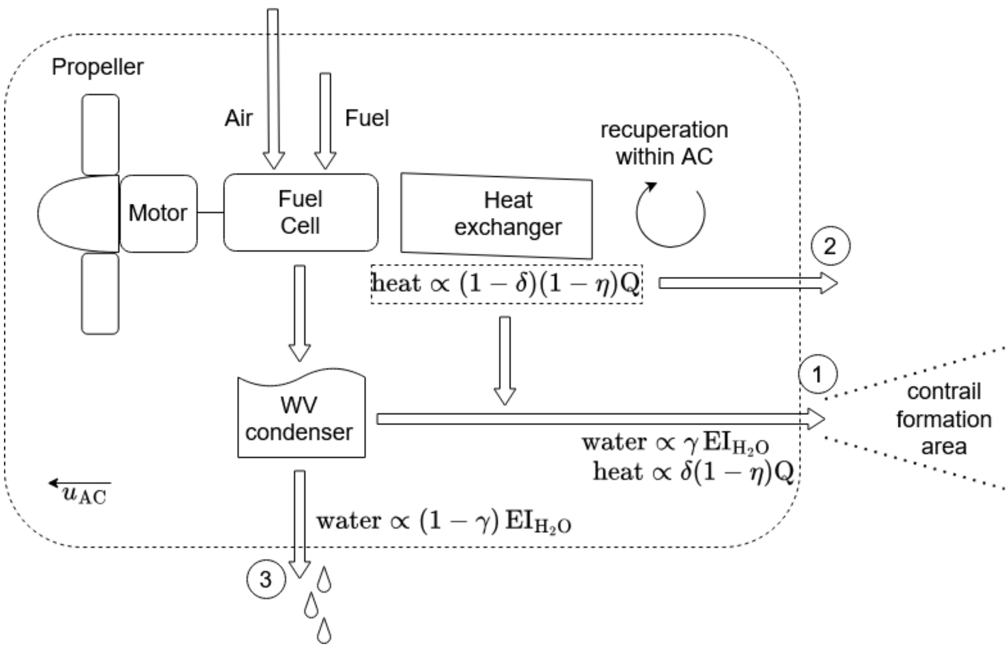

Figure 1. Schematic representation of contrail-relevant components of future FC-based propulsion system with thermal heat management and a water vapour condenser. The dashed boundary denotes the aircraft frame moving with the velocity u_{AC}, while the dotted lines illustrate the expanding exhaust plume. The arrows depict mass flows. To enhance clarity all arrows have the same width, yet this does not imply equal magnitude of all mass flow rates.
This figure has been adapted from Fig. 1b in Hillenbrand and Unterstrasser (2026).

$$\dot{m}_{\mathrm{E}} = \frac{p_{\mathrm{a}}}{R_{\mathrm{E}}\,T_{\mathrm{E}}} A_{\mathrm{E}}\,u_{\mathrm{E}}, \tag{5}$$

where R_{E} is the specific gas constant of the exhaust, A_{E} and u_{E} are the exhaust area and velocity, respectively. R_{E} can be expressed in terms of the universal gas constant R_{u} and the molar mass of the humid exhaust gas M_{E}:

$$R_{\mathrm{E}} = \frac{R_{\mathrm{u}}}{M_{\mathrm{E}}} = \frac{R_{\mathrm{u}}}{M_{\mathrm{da}} - q_{\mathrm{E}}(M_{\mathrm{da}} - M_{\mathrm{H_2O}})} \tag{6}$$

where M_{da} and $M_{\mathrm{H_2O}}$ are the molar mass of dry air and water, respectively. Substituting Eqs. (1), (2) and (6) into Eq. (5), explicitly expresses the exhaust mass flow in terms of the relative emission factors γ and δ:

$$\dot{m}_{\mathrm{E}} = \frac{p_{\mathrm{a}}\,A_{\mathrm{E}}\,u_{\mathrm{E}}\,c_p\,\mathcal{C}_{\mathrm{E}}}{R_u\left[T_{\mathrm{a}}\,c_p\,\mathcal{C}_{\mathrm{E}} + \delta\,Q(1-\eta)\right]}\left[M_{\mathrm{da}} - \gamma\frac{\mathrm{EI}_{\mathrm{H_2O}}}{\mathcal{C}_{\mathrm{E}}}(M_{\mathrm{da}} - M_{\mathrm{H_2O}})\right] \tag{7}$$

We assume that A_{E} and air-to-fuel ratio $\mathcal{C}_{\mathrm{E}}$ remain invariant under variations of γ and δ. Consequently, alterations in γ and/or δ change either the exhaust velocity u_{E} or mass flow $\dot{m}_{\mathrm{E}}$, according to Eq. (7). Theoretical considerations show that a

https://doi.org/10.5194/jecats-2026-16
Preprint. Discussion started: 25 August 2026

modification of the exhaust velocity changes the temperature evolution of the plume by an adaptation of the jet dilution rates (Zink and Unterstrasser, 2025). Lewellen (2020) and Zink and Unterstrasser (2025) derived scaling relations for contrail ice crystal number that capture the effect of modifications in u_E and/or A_E. These scaling relations are based on free jet theory by Pope (2000) and are only valid within the strong jet regime and for exhaust that is directly emitted into the free atmosphere. In the FC case, the exhaust may, however, be located such that the plume evolves close to the aircraft frame. Moreover, the swirling flow from the propellers may interact with the diluting exhaust. Hence, the scalings developed for H_2 combustion (Zink and Unterstrasser, 2025) are not applicable for H_2FC aircraft plumes. Taking this into account, we prefer to keep u_E constant in our setup. Then, variations of γ and δ imply a change of the exhaust mass flow $\dot{m}_\mathrm{E}$.

For conventional kerosene combustion engines, soot emissions (in terms of number per flown distance) scale with the exhaust mass flow and an increased exhaust mass flow results in more ice crystals (per flown distance). This is in contrast to FC propulsion systems, for which the exhaust is assumed to be free of any particles. Therefore, mass flow variations exhibit no direct influence on contrail formation behind H_2FC aircraft, as long as the exhaust velocity remains constant. Thus, for simplicity, we attribute reductions in heat and WV to changes in the exhaust mass flow, which has no direct effect for the contrail formation simulations in this study.

2.2 LCM box model

To investigate the influence of HDN on contrail formation behind H_2FC aircraft, we use the Lagrangian Cloud Module (LCM) in a box model version. The LCM has first been described in Sölch and Kärcher (2010). This model has been coupled with the large-eddy simulation (LES) model EULAG to investigate natural cirrus clouds (Sölch and Kärcher, 2011) and both young and aged contrails (Unterstrasser, 2014; Unterstrasser et al., 2017) in the past. The LCM box model variant used in this study captures the microphysics of contrail formation via the liquid phase, prescribing dynamic effects rather than solving the Navier-Stokes equations. This LCM box model is described in detail in Bier et al. (2022, 2024), where contrail formation on soot for kerosene combustion and on ambient aerosol for hydrogen combustion has been studied, respectively. Recently, this model has been used in (Zink et al., 2025b, a; Zink and Unterstrasser, 2025) to investigate various microphysical and engine-related aspects of contrail formation for hydrogen combustion.

We summarize the governing equations of the LCM box model that are essential for the analysis presented in this study. The initial thermodynamic exhaust properties q_E and T_E are given by Eqs. (1) and (2), respectively.

It is assumed that plume cooling occurs under isobaric, turbulent conditions, and that the temperature dependence of the heat capacity c_p can be neglected. Under these assumptions the temporal evolution of water vapour and temperature can be derived from the entrainment rate ω (Kärcher, 1995):

$$\frac{\mathrm{d}\alpha}{\mathrm{dt}} = -\omega(t)\,(\alpha(t) - \alpha_\mathrm{E}) + S_\alpha(t) \qquad \text{for } \alpha = \{\mathrm{T}, \chi_\mathrm{wv}\} \tag{8}$$

where $\chi_\mathrm{wv} = \rho_\mathrm{wv}/\rho_\mathrm{da}$ is the mass fraction of water vapour and S_α represent the source/sink terms due to latent heat and phase changes, respectively.

https://doi.org/10.5194/jecats-2026-16
Preprint. Discussion started: 25 August 2026

The turbulent plume leads to an identical ω for both WV and temperature. The entrainment rate of the exhaust plume can be calculated from the dilution factor $\mathcal{D}(t)$ as

$$\omega = -\frac{\mathrm{d}\ln\mathcal{D}}{\mathrm{dt}} \tag{9}$$

The time-dependent dilution of the plume $\mathcal{D}(t)$, representing the mass fraction of the exhaust in a plume parcel downstream of the engine, is given by

$$\mathcal{D}(t) = \frac{\mathcal{C}_\mathrm{E}+1}{\mathcal{C}(t)} \approx \frac{\mathcal{C}_\mathrm{E}}{\mathcal{C}(t)} \tag{10}$$

where $\mathcal{C}(t)$ is the temporal evolution of the air-to-fuel ratio during plume cooling. The approximation holds under the assumption that $\mathcal{C}_\mathrm{E} \gg 1$, which is valid due to typically large air-to-fuel ratios. For current kerosene combustion systems, $\mathcal{C}_\mathrm{E} \approx 50-70$ (Kärcher et al., 2015). These ratios might differ for H_2FC aircraft due to a different propulsion system design. If air and hydrogen react with a stoichiometric ratio of 1, the air-to-fuel ratio of the exhaust would be $\mathcal{C}_\mathrm{stoch} \approx 36$. While Chen et al. (2020) report optimal stoichiometric ratios within the range of $\sim 2-4$ depending on the operating conditions, aircraft applications usually use a stoichiometric ratio of ~ 1.5 (Zhang et al., 2024). This results in a theoretical air-to-fuel ratio range $\mathcal{C}_\mathrm{E} \approx 50-150$. Notably, $\mathcal{C}_\mathrm{E}$ can be larger if e.g. cooling air is mixed into the exhaust stream to reduce its humidity prior to emission. The dilution factor is, by definition, unity at the engine exit $\mathcal{D}(0) = 1$ and decreases monotonically with time as the plume mixes with the surrounding atmosphere.

The plume dynamics behind H_2FC aircraft exhibit distinct characteristics compared to those of conventional turbo-jet or turbo-fan plumes. The smaller exhaust area (compared to typical turbo-fan engines), the lower exhaust velocity and the turbulent motion induced by the propeller result in a more rapid plume dilution. In Appendix A, various dilution rates are introduced and compared. This dilution rate $\mathcal{D}$ used in this study as reference is based on a dedicated RANS simulation conducted for a H_2FC aircraft under conditions closely matching the reference values specified in Table 4.

The entrainment of ambient aerosols into the plume in terms of the dilution rate is described by

$$N_\mathrm{aero}(t) = n_\mathrm{aero} A_\mathrm{E} \frac{T_\mathrm{a}}{T_\mathrm{E}} \frac{u_\mathrm{tot,E}}{u_\mathrm{AC}} \left(\mathcal{D}^{-1}(t) - 1\right) \tag{11}$$

where $N_\mathrm{aero}(t)$ is the total number of aerosols entrained into the plume, while n_aero denotes the ambient aerosol number concentration and $u_\mathrm{tot,E} = u_\mathrm{E} + u_\mathrm{AC}$ is the total exhaust velocity (relative to the moving aircraft), which is the sum of the jet velocity u_E and the aircraft velocity u_AC (both defined relative to the background atmosphere).

Unlike Eulerian cloud microphysics models, the LCM employs a particle-based approach using simulation particles (SiPs) to track particles within the plume. Each SiP represents a certain number of real particles that share the same properties, such as radius, phase and particle type. The SiP properties change due to microphysical processes like hygroscopic growth and activation into water droplets, condensation growth, homogeneous freezing of supercooled droplets, depositional ice crystal growth

https://doi.org/10.5194/jecats-2026-16
Preprint. Discussion started: 25 August 2026

and latent heat release. Additionally, we allow for droplets to be formed inside the plume during the simulation by HDN. The physical aspects of this microphysical process and its implementation are given in Sec. 3.

The main result of an LCM box model simulation is the number of formed ice crystals N_{ice}. This quantity is given per flight meter along the flight direction as it is crucial for the radiative effect associated with the evolving contrail-cirrus (Lottermoser and Unterstrasser, 2026). $N_{\mathrm{ice}}(t)$ is monotonically increasing and reaches a constant value once the plume is no longer supersaturated with respect to water and freezing is completed. The asymptotic value at this stage is defined as the final ice crystal number $N_{\mathrm{ice,f}}$.

3 Homogeneous Droplet Nucleation

3.1 Theoretical background

This section deals with the extension of the LCM box model to incorporate the formation of pure water droplets via Homogeneous Droplet Nucleation. HDN is the process by which water droplets are formed directly from the vapour phase, without the need for any condensation nuclei. HDN does not occur under atmospheric conditions, as extremely high levels of relative humidity ($\mathrm{RH_w} \gtrsim 500\,\%$) are necessary to generate a significant amount of water droplets at low temperatures. Nevertheless, there are some technical applications that create conditions that trigger HDN, such as turbo chargers (Wittmann et al., 2021) or steam turbines (Bakhtar et al., 2005). Furthermore, Jansen and Heymsfield (2015) showed that aerodynamic contrails occurring in very cold and/or humid ambient conditions are formed via HDN.

Becker and Döring (1935) were the first to describe HDN analytically by calculating the smallest stable cluster of water molecules in a given supersaturated environment. Their derivation is based on classical nucleation theory and a detailed explanation is given in Bakhtar et al. (2005). A droplet is considered stable if its radius r exceeds a critical radius $r^\star$ which coincides with the maximum value of the Gibbs free energy ΔG of a formed droplet. The radius of such a single critical cluster of water molecules can be calculated from the Gibbs-Thompson equation as

$$r^\star = 2\frac{v_{\mathrm{m}}\sigma}{k_{\mathrm{B}}T\ln(S)} \tag{12}$$

where σ is the surface tension of the critical cluster and v_{m} its molecular volume, while S is the supersaturation value and k_{B} is the Boltzmann constant. Droplets with $r < r^\star$ are considered unstable and evaporate directly after their formation. Conversely, droplets with $r > r^\star$ are stable for constant surrounding conditions and grow by diffusion. With increasing supersaturation the higher number concentration of water vapour molecules increases the probability of collisions by Brownian motion leading to the formation of stable droplets. Another effect of increased supersaturation is that $r^\star$ decreases and fewer molecules are necessary to form a stable droplet. Both effects favour droplet formation via HDN at high supersaturation values, leading to a non-linear increase in the nucleation rate J_{HDN} with increasing supersaturation. When using classical nucleation theory, this

https://doi.org/10.5194/jecats-2026-16
Preprint. Discussion started: 25 August 2026

	Case 1	Case 2	Case 3
Temperature T/ K	250	249.9	250.1
Supersaturation S	6	6.05	5.95
Relative J_{BD}	1	1.57	0.63

Table 2. Exemplary nucleation rates for a temperature $T = 250$ K and $S = 6$ and and their variation for $\Delta T = \pm 0.1\mathrm{K}$ assuming the same amount of WV.

rate can be expressed as (Becker and Döring, 1935):

$$J_{\mathrm{BD}} = \sqrt{\frac{2\sigma}{\pi m_{\mathrm{m}}}} v_{\mathrm{m}} \left(\frac{p_{\mathrm{wv}}}{k_{\mathrm{B}}T}\right)^2 \exp\left\{\frac{-16\pi v_{\mathrm{m}}^2 \sigma^3}{3(k_{\mathrm{B}}T)^3(\ln S)^2}\right\}, \tag{13}$$

where m_{m} is the mass of one water molecule and p_{wv} the actual WV pressure. Note that the classical rate J_{BD} is physically sensible only for supersaturated environments (i.e $S > 1$).

The strong non-linearity of the classical nucleation rate J_{BD} is shown by evaluating Eq. (13) for conditions representative for a moist aircraft plume. If ambient conditions support contrail formation, aircraft plumes become supersaturated for $T < 270\,\mathrm{K}$. Let's assume $T_0 = 250\,\mathrm{K}$ and a supersaturation value $S_0 = 6 = 600\,\%$. A small perturbation $\Delta T = \pm 0.1\,\mathrm{K}$ leads to a supersaturation deviation of approximately ± 0.05 for a fixed absolute WV amount (Table 2). Evaluating Eq. (13) reveals that the corresponding nucleation rate ratio is larger by a factor of 1.57 in the lower-temperature case (Case 2) and smaller by a factor of 0.63 in the higher-temperature case (Case 3). This simple example shows that small deviations in temperature and supersaturation can lead to substantial changes in the nucleation rate and consequently in the number of formed droplets.
Various experimental data show discrepancies between measured nucleation rates and the theoretically predicted nucleation rate J_{BD}. Therefore, several corrections of J_{BD} have been suggested to fit the experimental nucleation rates more accurately. One of the most frequently used corrections is given in Kantrowitz (1951), accounting for the higher temperature of the formed droplet compared to its surrounding conditions due to the release of latent heat. This correction reduces the nucleation rate by approximately two orders of magnitude and is used in many numerical models for steam applications (Starzmann et al., 2018).
The nucleation rate J_{Kan} relies purely on theoretical corrections and Kantrowitz (1951) gives no limiting conditions for its usage:

$$J_{\mathrm{Kan}} = \frac{J_{\mathrm{BD}}}{1+\phi} \text{ with } \phi = \frac{2(\kappa - 1)}{\kappa + 1} \frac{L_{\mathrm{H}}}{R_{\mathrm{wv}}T} \left(\frac{L_{\mathrm{H}}}{R_{\mathrm{wv}}T} - \frac{1}{2}\right) \tag{14}$$

where $\kappa = 1.4$ is the isentropic expansion coefficient of air and L_{H} is the latent heat of condensation.
Another, empirical, correction has been proposed by Wölk et al. (2002). Their results for the nucleation rate are compared to various measurements in Fig. 3 in Jansen and Heymsfield (2015) and yield accurate results for $200\,\mathrm{K} < T < 270\,\mathrm{K}$, which fits the supersaturated conditions in aircraft plumes. Their final empirical nucleation rate J_{WS} can be calculated from the theoretical rate J_{BD} as

https://doi.org/10.5194/jecats-2026-16
Preprint. Discussion started: 25 August 2026

$$J_{\mathrm{WS}} = J_{\mathrm{BD}}\,\exp\left\{-27.56 + \frac{6.5\cdot 10^{-3}}{T}\right\}. \tag{15}$$

3.2 Implementation in LCM box model

In this section, the implementation of droplet creation via HDN within the LCM box model is described in more detail and convergence tests are used to show numerical convergence for the implemented process.

The various processes in the box model are implemented using operator splitting. In particular, nucleation and diffusional growth processes are not solved simultaneously, but are treated separately in consecutive order in each time step.

During plume cooling the HDN nucleation rate J_{HDN} increases in a highly non-linear fashion until the peak relative humidity value $\mathrm{RH}_{\mathrm{w,max}}$ is reached, see Fig. 5b. After $\mathrm{RH}_{\mathrm{w,max}}$ is reached, J_{HDN} drops rapidly. For the temperature range, where aircraft plumes are typically supersaturated (i.e. $T \lessapprox 270\,\mathrm{K}$), the HDN process becomes relevant only for $\mathrm{RH}_{\mathrm{w}} > 500\%$. Consequently, for the majority of time steps J_{HDN} is negligibly small and we do not need to consider droplet formation via HDN. To account for this, we introduce a threshold $J^{\star}_{\mathrm{HDN}}$ as a critical minimum nucleation rate, below which droplet formation by HDN is neglected. For the minimum critical threshold a constant value of $J^{\star}_{\mathrm{HDN}} = 10^{2}(\mathrm{m}^{3}\mathrm{s})^{-1}$ is chosen. The time step used in the LCM box model is typically $\Delta t_{\mathrm{LCM}} \leq 10^{-3}\,\mathrm{s}$ and a representative plume area is on the order of $1\,\mathrm{m}^{2}$. leads to neglecting less than one water droplet formed per time step. Under these conditions, the expected number of droplets formed per time step $n_{\mathrm{drp}} = J_{\mathrm{HDN}}\,\Delta t_{\mathrm{LCM}}\,A_{\mathrm{plume}}$ is less than one when the nucleation rate is below the threshold. If $J_{\mathrm{HDN}} > J^{\star}_{\mathrm{HDN}}$, a time step refinement is applied, refining Δt_{LCM} by the factor n_{fine} to $\Delta t_{\mathrm{fine}} = \Delta t_{\mathrm{LCM}}/n_{\mathrm{fine}}$.

In each refined time step, a single SiP is initialized, which represents $n_{\mathrm{HDN}} = J_{\mathrm{HDN}}\,A_{\mathrm{plume}}\,\Delta t_{\mathrm{fine}}$ droplets. We prescribe the critical radius $r^{\star}$ via Eq. (12) as the initial SiP radius because this represents the smallest droplet that is stable under the current conditions. For the model to be consistent with Eq. (8), mass fraction changes by condensation and temperature changes by latent heat release are accounted for each SIP creation.

Numerical convergence tests have been performed for Δt_{fine} using the most demanding case presented in Sec. 4. In this context, 'demanding' refers to the generation of a large number of droplets by HDN due to large supersaturation values in the plume. The highest number of droplets is formed, when the fast dilution rate $\mathcal{D}_{\mathrm{Neph}}$ (see Appendix A and (Braun et al., 2026)) is used. The other parameters are set to their reference values given in Table 4, using the highest amount of WV in the exhaust, i.e. $\gamma = 1$.

Fig. 2a shows the final ice crystal number $N_{\mathrm{ice,f}}$ per flight meter for different time steps Δt_{fine}, taking droplet creation by HDN into account. For better visual differentiation, both colour and marker style illustrate the different order of diffusion and nucleation process within one time step. Both variants converge for decreasing Δt_{fine} to the same $N_{\mathrm{ice,f}}$. Higher temporal resolution, i.e. lower Δt_{fine}, is expected to yield more accurate simulation results. In this study, we consider the simulation performed with $\Delta t_{\mathrm{fine}} = 0.005\,\mu\mathrm{s}$ to represent the most resolved and thus most reliable reference solution. Fig. 2a shows that the implementation of first accounting for nucleation and then for diffusion leads to more accurate results for larger Δt_{fine} during the HDN process. Therefore, the nucleation of water droplets is implemented to take place before the diffusion process within one time step. The relative difference of the simulation using $\Delta t_{\mathrm{fine}} = 0.5\,\mu\mathrm{s}$ to the finest resolution is less than 3%.

https://doi.org/10.5194/jecats-2026-16
Preprint. Discussion started: 25 August 2026

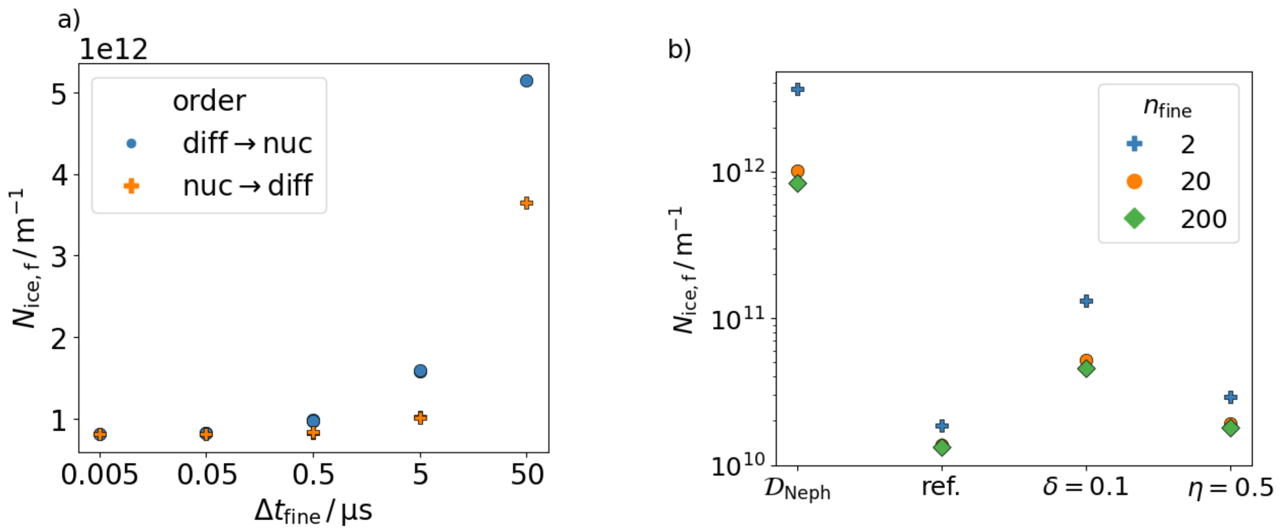

Figure 2. Temporal convergence of $N_{\mathrm{ice,f}}$.
a) Variation of Δt_{fine} and comparison of the order of nucleation and diffusion process. The investigated setup uses the parameters for the reference case, given in Table 4 with $\gamma = 1$, except that the dilution rate $\mathcal{D}_{\mathrm{Neph}}$ (Braun et al., 2026) is used. b) Temporal convergence for various setups from Sec. 4.1 using $\Delta t_{\mathrm{LCM}} = 10^{-4}\,\mathrm{s}$, while varying n_{fine}. The x-axis labels indicate the parameter that differs from the reference case given in Table 4.

Thus, we conclude that using $\Delta t_{\mathrm{fine}} = 0.5\,\mu\mathrm{s}$ is sufficiently small to achieve accurate results even for demanding nucleation scenarios.

Fig. 2b supports this choice by showing the convergence of $N_{\mathrm{ice,f}}$ with n_{fine} when using $\Delta t_{\mathrm{LCM}} = 10^{-4}\,\mathrm{s}$ for various contrail formation scenarios. Both, Fig. 2a and 2b show that for increasing n_{fine}, $N_{\mathrm{ice,f}}$ decreases. For small n_{fine}, the peak nucleation rate $J_{\mathrm{HDN,max}}$ is slightly over-predicted due to a coarser temporal resolution of the temperature evolution, which leads to an increased HDN rate as shown by Case 2 in Table 2. This increased HDN rate consecutively leads to increased $N_{\mathrm{ice,f}}$.

Note that an increase in n_{fine} does not result in a linear increase in computation time, because the time step refinement is only applied for a small number of box model time stamps for which HDN forms a relevant number of droplets. Therefore, the time step $\Delta t_{\mathrm{LCM}} = 10^{-4}\,\mathrm{s}$ together with the refinement $n_{\mathrm{fine}} = 200$ is chosen for all simulations to ensure accurate results for all contrail formation scenarios in this publication.

3.3 Validation

Previous research has extensively employed the LCM box model, for example in (Kärcher, 1995; Bier et al., 2022, 2024). The capability of the growth and freezing equations implemented in the box model to accurately capture the microphysical behavior of very small droplets is described in Appendix B. Consequently, the validation focuses on the modifications related to the implementation of the HDN process and its effect on the temperature evolution by latent heat generation.

https://doi.org/10.5194/jecats-2026-16
Preprint. Discussion started: 25 August 2026

We validate the HDN implementation in the LCM box model against a benchmark testcase employed for CFD simulations for steam applications, described in Starzmann et al. (2018). In this publication, 13 distinct Computational Fluid Dynamics (CFD) codes were applied to different converging-diverging nozzle test cases from the International Wet Steam Modeling Project. The flow field is characterized by a turbulent, supersonic vapour flow accelerated within the nozzle by adiabatic expansion. During the expansion of the steam, the rapid decrease of pressure and temperature leads to supersaturated conditions that eventually trigger homogeneous nucleation of liquid water droplets from the vapour phase. The subsequent condensation process releases latent heat, resulting in a localized increase in both temperature and pressure. Experimental measurements of the axial pressure evolution and the droplet size are available for some nozzles and serve as validation targets for numerical simulations.

We select the so-called 'Mystery nozzle' test case in Starzmann et al. (2018) for validation. This configuration features a nearly one-dimensional flow with a constant expansion rate, minimizing complex boundary layer interactions and secondary flow effects present in other nozzle setups. The small influence of the dynamics is ideal to validate the LCM box model that does not simulate the flow dynamics explicitly. Although experimental data is not available for the Mystery nozzle, inter-code consistency assessment provides a robust basis for validating the implementation of HDN in the box model.

3.3.1 Test case setup

The flow dynamics of the nozzle test cases are governed by different physical processes than the dilution of an aircraft plume. Rather than directly solving Eq. (8), the expansion process within the nozzle is decomposed into two sequential steps for each timestep: an adiabatic phase and a microphysically driven correction. Intermediate variables, denoted with an asterisk, are introduced for temperature and pressure, representing the state of the flow prior to the incorporation of microphysical effects. These intermediate variables after adiabatic expansion $p_\mathrm{i}^\star$ and $T_\mathrm{i}^\star$ are calculated by:

$$p_\mathrm{i}^\star = p_{\mathrm{i}-1} \exp\left\{-\dot{P}\Delta t\right\} \tag{16}$$

$$T_\mathrm{i}^\star = T_{\mathrm{i}-1} \left(\frac{p_\mathrm{i}}{p_{\mathrm{i}-1}}\right)^{\frac{\kappa-1}{\kappa}} \tag{17}$$

Afterwards, Eqs. (8) are solved for both q and T, with $\omega(t) = 0$, as no entrainment into the nozzle takes place. The specific humidity only changes by condensation, evaporation and condensational growth. These microphysical processes release latent heat, changing the temperature, thereby inducing non-adiabatic temperature changes. To account for the effect of potential temperature changes, the pressure is updated afterwards using the ideal gas law:

$$p_\mathrm{i} = p_\mathrm{i}^\star \frac{T_\mathrm{i}}{T_\mathrm{i}^\star} \tag{18}$$

The adiabatic coefficient $\kappa = 1.32$ and the expansion rate of the nozzle $\dot{P} = 3400\,\mathrm{Pa/s}$ are treated as constant throughout the simulation. While Starzmann et al. (2018) report an expansion rate of $\dot{P} = 3500\,\mathrm{Pa/s}$, blockage due to boundary layers reduce the effective expansion rate to approximately $\dot{P} \approx 3400\,\mathrm{Pa/s}$. It should be noted that our approach neglects boundary wall effects and the dynamical influence of droplet formation on the flow, which are usually associated with a decrease in velocity.

https://doi.org/10.5194/jecats-2026-16
Preprint. Discussion started: 25 August 2026

	T_{inl} / K	p_{inl} / hPa	T_0 / K	p_0 / hPa
test case 1	417	1100	361.68	606.98
test case 2	388	1100	337.54	608.63

Table 3. Inlet conditions $T_{\mathrm{inl}}, p_{\mathrm{inl}}$ and initial values T_0, p_0 for the Mystery nozzle test cases from Starzmann et al. (2018).

The Mystery Nozzle, originally presented in Starzmann et al. (2018), is axisymmetric along its center line and the throat height (smallest cross section) is $h_0 = 40\,\mathrm{mm}$. The data sets presented in Starzmann et al. (2018) include values up to $35\,\mathrm{cm}$ behind the nozzle's throat, which corresponds to a simulation time of approximately $500\,\mathrm{\mu s}$. To account for these short timescales due to the supersonic flow, the simulation setup uses a constant time step of $\Delta t_{\mathrm{LCM}} = 0.1\,\mathrm{\mu s}$. The simulations are initialized such that $t_0 = 0\,\mathrm{s}$ corresponds to the time when the flow passes through the nozzle throat with Mach number $\mathrm{Ma} = 1$. Therefore, the initial conditions for our setup T_0, p_0 differ from the initial conditions at the inlet of the nozzle $T_{\mathrm{inl}}, p_{\mathrm{inl}}$ upstream of the throat. The inlet conditions for the two test cases with the corresponding initial conditions for the box model simulations are given in Table 3. Initially, the flow consists of pure WV, giving $p_{\mathrm{wv},0} = p_{\mathrm{inl}}$, without any droplets or other particles. We assume homogeneous conditions within each cross section of the nozzle. Once the supersaturation is large enough to trigger HDN, water droplets are generated via the HDN process. As the temperature values for the nozzle test cases exceed the validity range of the nucleation rate by Wölk et al. (2002), the more general correction J_{Kan} is used for the validation. These droplets then grow by condensation and further decrease the supersaturation. Both droplet formation by HDN and condensational growth increase the temperature by latent heat.

3.3.2 Test case results

The temporal evolution of key properties of the nozzle test case are displayed along its center line in Starzmann et al. (2018). Consistent with the Lagrangian framework of our model, we show the respective results relative to the mean flow passage time at the nozzle throat. We compare the temperature and droplet size evolutions for the two nozzle configurations detailed in Table 3. The droplet size evolution presented in Starzmann et al. (2018) show either the Sauter radius r_{32} or the mean radius $\bar{r}$ depending on the CFD model. The mean Sauter radius of a droplet distribution corresponds to the effective radius defined in Eq. (21) of Bier et al. (2022). The typically narrow droplet size distribution generated by HDN leads to small deviations between the Sauter and the mean radius as displayed in Fig. 12 of Starzmann et al. (2018).

Figs. 3a and 3b present the temporal evolution of flow temperature for both initial conditions. The gray lines denote results from all CFD codes reported in Starzmann et al. (2018), while the black lines correspond to the LCM box model simulation results. The surface tension σ_{ref} is computed using the formulation from Wölk and Strey (2001), which deviates from the IAPWS-95 definition (IAPWS, 1995) by less than $0.5\,\%$ across the relevant temperature range $T \in [220, 400]$ K. While the solid black line represents the baseline case $\sigma = \sigma_{\mathrm{ref}}$, the dotted and dashed lines correspond to $\sigma = 1.05\,\sigma_{\mathrm{ref}}$ and $\sigma = 0.95\,\sigma_{\mathrm{ref}}$, respectively. The adapted surface tension values cover the full range of σ values used in the participating CFD codes of the original study. Their effect on the test case results is shown in Fig. 15 of Starzmann et al. (2018). For both initial conditions, a

https://doi.org/10.5194/jecats-2026-16
Preprint. Discussion started: 25 August 2026

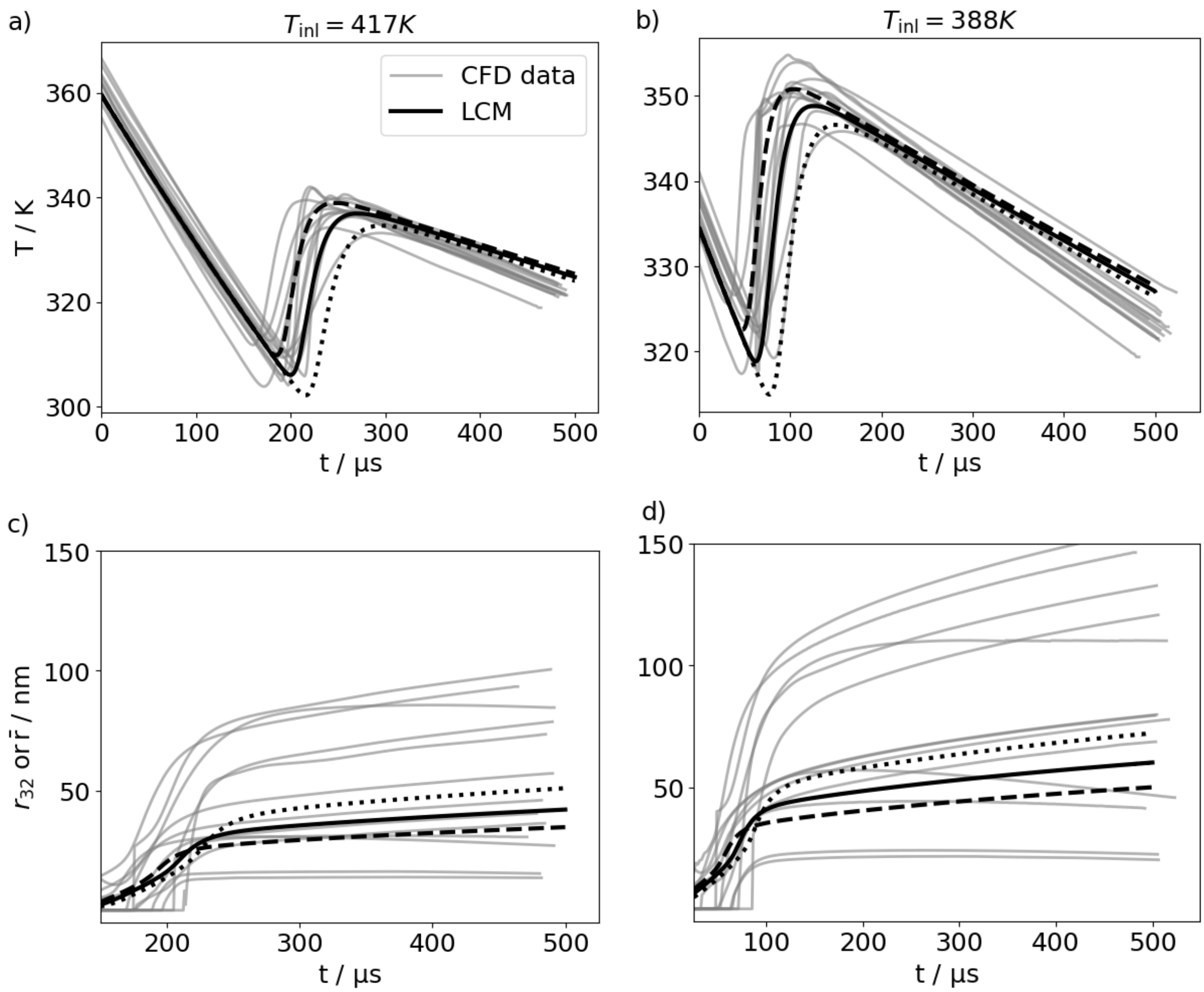

Figure 3. Temperature (a and b) and droplet size (c and d) evolution for the test case 'Mystery nozzle' from Starzmann et al. (2018). The initial temperature is $T_{\text{inl}} = 417\,\text{K}$ in a and c; and $T_{\text{inl}} = 388\,\text{K}$ in b and d. The gray lines denote the results of various CFD codes, presented in the original study, while the black lines show the evolution using the LCM box model for various surface tension values: solid: $\sigma = \sigma_{\text{ref}}$, dotted: $\sigma = 1.05\,\sigma_{\text{ref}}$, dashed: $\sigma = 0.95\,\sigma_{\text{ref}}$.

higher surface tension results in a delayed temperature increase with no long-lasting influence. The LCM box model demonstrates excellent agreement with CFD data, accurately capturing both the onset of HDN and the latent heat-driven temperature increase.

Accurate simulation of droplet creation via HDN requires precise modeling of both temperature and droplet size evolution (Starzmann et al., 2018). Consequently, Figs. 3c and 3d illustrate the temporal evolution of droplet size for both initial temperature values with black lines denoting surface tension variations analogous to Figs. 3a and 3b. At nucleation onset an increased surface tension yields smaller droplets due to delayed nucleation, while final droplet sizes at the nozzle exit exceed baseline

https://doi.org/10.5194/jecats-2026-16
Preprint. Discussion started: 25 August 2026

values. This trend arises because increased surface tension leads to a reduced nucleation rate, see Eq. (13), resulting in fewer droplets that can grow larger by reducing the supersaturation. Again, the results from the LCM box model consistently fall within the range of all CFD codes with final droplet sizes positioned at the lower end of the range. This is expected because models based on monodispersed droplet distributions tend to over-predict droplet sizes compared to discrete-spectrum approaches (such as the LCM box model) (Starzmann et al., 2018).

This sections validates the implementation of HDN in the box model. We demonstrate that simulation results align with multiple CFD models for two distinct nozzle test cases. While the thermodynamic properties of the steam flow in these validation cases do not represent typical aircraft plumes — due to higher nucleation onset temperatures — the resulting elevated nucleation rates create demanding test conditions for the box model. Consequently, successful simulation of these challenging cases confirms the model's capability to accurately capture nucleation processes in aircraft plumes.

4 Simulation results

4.1 Simulation setup

We perform simulations with the LCM box model, described in Sec. 2, to conduct a systematic investigation of the HDN effect in plumes generated by H_2FC aircraft. Table 4 summarizes key parameters of the simulation setup within this study. The parameters for the reference case are marked with an asterisk and will be motivated in the following.

The ambient pressure $p_\mathrm{a} = 300\,\mathrm{hPa}$ corresponds approximately to FL 300 according to the International Standard Atmosphere (ISA). This flight altitude lies within the range of relevant cruise altitudes for regional aircraft, that commonly fly between FL 300 and FL 270. The ambient temperature is set to $T_\mathrm{a} = T_\mathrm{ISA} - 10\,\mathrm{K} = 218.7\,\mathrm{K}$. The focus on cold conditions is motivated by their tendency to promote high supersaturation values during cooling, which in turn leads to higher HDN rates. A saturated atmosphere with relative humidity over ice $\mathrm{RH}_\mathrm{i,a} = 100\,\%$ is assumed to exclude any effects of $\mathrm{RH}_\mathrm{i,a}$ on the simulation results. Regarding ambient aerosol properties, constant values are used for the number concentration $n_\mathrm{aero} = 100\,\mathrm{cm}^{-3}$ and the mean radius of the aerosol distribution $\bar{r}_\mathrm{aero} = 15\,\mathrm{nm}$ in agreement with the recent study by Zink et al. (2025b). The choice of n_aero lies well in between the reported aerosol number concentrations, ranging from $\sim 10^2 - 10^4\,\mathrm{cm}^{-3}$ (Petzold et al., 2002; Brock et al., 2021).

The FC exhaust is assumed to have a circular shape and its radius is set to $r_\mathrm{E} = 0.2\,\mathrm{m}$, such that the exhaust area is equivalent to the one defined by the original CFD simulation, from which the dilution data is deduced. As discussed in Sec. 2.1, the simulation results for H_2FC aircraft are independent of the exhaust mass flow rate $\dot{m}_\mathrm{E}$ as long as its variation does not influence the exhaust velocity, changing the dilution rate. For the sake of completeness, a hydrogen mass flow rate of $\dot{m}_{\mathrm{H}_2} = 0.046\,\mathrm{kg/s}$, representative for the baseline conditions reported in the DLR EXACT project (Atanasov and Silberhorn, 2025). Following the methodology outlined in Hillenbrand and Unterstrasser (2026), the thermodynamic exhaust properties are defined by specifying the overall propulsion efficiency η, the initial air-to-fuel ratio $\mathcal{C}_\mathrm{E}$ and the relative WV and heat emission factors γ and δ, see Eqs. (1) and (2). In line with expected efficiencies for future H_2FC aircraft (Frey et al., 2025) the overall efficiency is set to $\eta = 0.4$. The initial air-to-fuel ratio state of the exhaust is set to $\mathcal{C}_\mathrm{E} = 100$, which is in line with expected air-to-fuel ratios for

https://doi.org/10.5194/jecats-2026-16
Preprint. Discussion started: 25 August 2026

FC operating conditions (Chen et al., 2020). These specifications, along with the heat emission factor δ determine the exhaust temperature of the H_2FC aircraft. By selecting $\delta = 0.2$, corresponding to $80\,\%$ heat separation, the exhaust temperature is $T_E \approx 355\,K$, falling within the operating range of PEM-FC systems (Frey et al., 2025). Currently, there are no concrete design concepts for integrating WV reduction systems into H_2FC aircraft. To explore the influence of such systems on the occurrence and impact of HDN on ice crystal formation, we vary the WV emission factor $\gamma \in [0.2, 1]$, creating a simulation set of five cases, referred to as the 'reference case'. The exhaust is assumed to be void of any particles, restricting droplet formation to two mechanisms: nucleation on entrained ambient aerosols and HDN. Subsequently, droplets grow via condensation and freeze into ice crystals once the plume temperature drops below their respective freezing thresholds.

We employ a maximum simulation time of $t_{sim} = 3\,s$ for all simulations with a general time step $\Delta t_{LCM} = 10^{-4}\,s$. When HDN is relevant, the time step is refined by a factor of $n_{fine} = 200$ as detailed in Sec. 3.2. The nucleation rate due to HDN is calculated using the empirical correction proposed by Wölk et al. (2002), as this parametrization is well-suited for the temperature and saturation conditions typically encountered in aircraft plumes.

We emphasize that the parameters describing the exhaust conditions can be chosen differently due to the variability in potential future H_2FC aircraft designs. To account for these various uncertainties, several parameters have been varied from their reference case value, indicated in Table 4. Each parameter is varied individually to assess its impact on ice formation. The ambient parameters modified include ambient temperature, pressure, and the number concentration of ambient aerosols. The plume dilution rate is also varied, considering both stronger and weaker dilution scenarios relative to the reference dilution $\mathcal{D}$, specified in Appendix A. Additionally, the overall propulsion efficiency is increased to reflect potential future improvements. The heat emission factor is further reduced to $\delta = 0.1$, representing colder exhausts that can be associated with low-temperature PEM-FCs. To address uncertainties in the HDN rate parametrization, additional simulations are conducted using the parametrization by Kantrowitz (1951) as well as different values of the surface tension σ, as discussed in Sec. 3.3.2.

4.2 Relevance of exhaust humidity on HDN process

Simulations were performed for WV emission factors ranging from $\gamma = 1$ to $\gamma = 0.2$ to cover a broad spectrum of exhaust conditions. Fig. 4a shows the SAC mixing lines for several γ values in a so-called Schmidt-Appleman diagram, relating the plume's temperature to its WV partial pressure (as established in Schumann, 1996). The gray curve denotes the WV saturation pressure. Simulation results are shown in colour, while the black dashed lines represent the corresponding SAC mixing lines. The initial WV partial pressure in the exhaust, indicated by coloured stars in the upper right of Fig. 4a, is directly proportional to γ. As the plume mixes with the ambient air, its thermodynamic state evolves along these curves relaxing to the ambient conditions, represented by the black point in the lower left. Fig. 4b displays RH_w over T_{plume} for the same set of simulations. For $\gamma = 0.2$, the exhaust contains the least amount of WV. In this case, the simulation results closely follow the SAC mixing lines, as the limited number of entrained ambient aerosols is insufficient to effectively deplete supersaturation. $RH_{w,max}$ for this case is about $500\,\%$, remaining below the threshold required to trigger HDN. For $\gamma = \{0.6, 1\}$, higher plume supersaturation values are reached and HDN is initiated. Right after the onset of HDN, many droplets form rapidly. This process takes up substantial amounts of WV in a very short time period, causing a sharp reduction in supersaturation and $RH_{w,max}$ remains

https://doi.org/10.5194/jecats-2026-16
Preprint. Discussion started: 25 August 2026

Simulation parameter	Parameter values
Ambient conditions	
Temperature T_a	$T_\mathrm{ISA} - \{0, 5, 10^\star, 15, 20\}$ K
Pressure p_a / hPa	$\{300^\star, 350\}$
Relative humidity over ice $\mathrm{RH_{i,a}}$ / %	$100^\star$
Number concentration n_aero / cm^{-3}	$\{10, 100^\star, 1000\}$
Mean radius $\bar{r}_\mathrm{aero}$ / nm	$15^\star$
Exhaust properties	
Overall efficiency η	$\{0.4^\star, 0.5\}$
Fuel mass flow $\dot{m}_{\mathrm{H_2}}$ / $\mathrm{kg\,s^{-1}}$	$0.046^\star$
Exhaust radius r_E / m	$0.2^\star$
WV emission factor γ	$\{0.2, 0.4, 0.6, 0.8, 1\}^\star$
Heat emission factor δ	$\{0.1, 0.2^\star, 0.3\}$
Plume dilution	
Initial air-to-fuel ratio $\mathcal{C}_\mathrm{E}$	$\{50, 100^\star, 200\}$
Dilution rate $\mathcal{D}(t)$	$\{\mathcal{D}^\star, \mathcal{D}_\mathrm{Neph}, \mathcal{D}_\mathrm{Flud}\}$
HDN parametrization	
HDN rate parametrization	WS*, Kantro
Surface tension σ	$\{0.95\,\sigma_\mathrm{ref}, \sigma^\star_\mathrm{ref}, 1.05\,\sigma_\mathrm{ref}\}$

Table 4. Overview of simulation parameters relevant for contrail formation. Values marked with an asterisk indicate the reference value.

well below the the one derived from the SAC mixing line. Concurrently, the release of latent heat delays plume cooling. This results in distinct kinks in the simulated $p_\mathrm{wv}(T_\mathrm{plume})$ and $\mathrm{RH_w}(\mathrm{T_{plume}})$ relations.

The influence of initial plume WV content, quantified by γ, on the onset and strength of HDN is systematically examined in Fig. 5. It depicts the temporal evolution of $T_\mathrm{plume}, \mathrm{RH_w}$, HDN rate J_HDN and the total number of water droplets and ice crystals. The short time window up to $0.3\,\mathrm{s}$ after emission captures the complete HDN event, which can occur within a few milliseconds after emission. The black crosses in Fig. 5d indicate the first time step at which droplets freeze into ice crystals. For low $\gamma = \{0.2, 0.4\}$ HDN has no significant impact. The temperature decreases monotonically towards T_a, while $\mathrm{RH_w}$ increases up to its peak value and then slowly decreases. The peak HDN rate remains insufficient to generate a significant number of droplets, leading to a continuous increase of ice crystal numbers by the activation and freezing of entrained aerosols. Shortly after $t = 0.1\,\mathrm{s}$, N_ice for $\gamma = 0.4$ increases slightly compared to $\gamma = 0.2$, reflecting the small contribution of HDN-formed droplets that subsequently freeze. However, this difference diminishes and becomes negligible as the plume dilutes further. As γ increases, the number of water droplets increases rapidly within the first $0.1\,\mathrm{s}$ after emission and stays constant afterwards. The sharp increase of water droplet number is due to the HDN process which is driven by high supersaturation values. The increasing impact of HDN with rising γ is further evident in Fig. 5a, where the deviations of the temperature

https://doi.org/10.5194/jecats-2026-16
Preprint. Discussion started: 25 August 2026

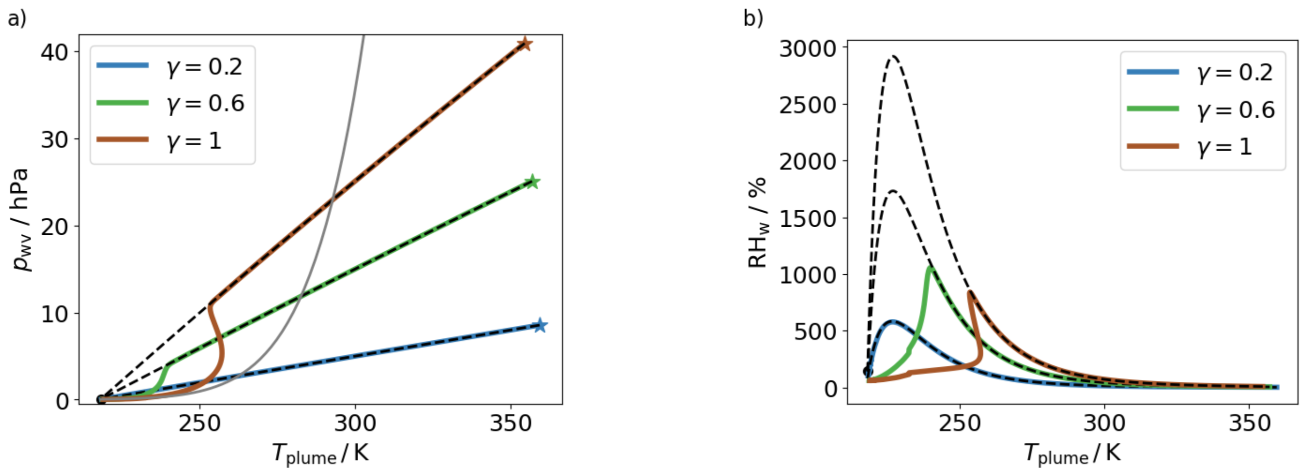

Figure 4. Comparison between SAC mixing line (black dashed curves) and microphysical simulations shown for different values of γ. Note that the plume conditions start at the right of the plots and go in negative x-direction towards ambient conditions on the left. a) p_{wv} over plume temperature. b) $\mathrm{RH_w}$ over plume temperature.

evolution, as derived purely from the prescribed dilution, become more pronounced the higher γ is. For $\gamma = 1$, the latent heat on HDN-formed droplets temporarily outweighs the cooling effect of dilution, resulting in a small temperature increase. The strong latent heating leads to a more pronounced peak in the relative humidity for higher γ values (Fig. 5b). Increased γ values lead to earlier onset of HDN at higher temperatures (cf. Fig. 5b) and lower relative humidity values. This leads to increased peak HDN rates for increased γ values despite decreasing $\mathrm{RH_{w,max}}$. A direct comparison between Fig. 5c and Fig. 5d reveals that higher peak HDN rates correspond to larger $N_{\mathrm{ice,f}}$ for high γ values.

Notably, for low γ the ice crystal number concentrations are too low to effectively deplete supersaturation depletion within the displayed time window. Consequently, N_{ice} increases beyond $t = 0.3\,\mathrm{s}$ by continuous entrainment, activation and freezing of ambient aerosols. Taking this into account, the relative increase in $N_{\mathrm{ice,f}}$ for higher γ values is not as pronounced as indicated in Fig. 5d. With the assumed ambient aerosol concentration $n_{\mathrm{aero}} = 100\,\mathrm{cm}^{-3}$, aerosol activation leads to $N_{\mathrm{ice,f}} \approx 2 \cdot 10^9\,\mathrm{m}^{-1}$ for low γ.

Overall, Fig. 5 demonstrates a positive correlation between exhaust WV content (quantified by γ) and the number of droplets formed via HDN. Therefore, actively reducing WV in the exhaust by technical means can effectively suppress HDN initiation, thereby reducing the number of ice crystals in contrails behind H_2FC aircraft. A general comparison of N_{ice} behind H_2FC aircraft and kerosene combustion aircraft is given in Sec. 5.

4.3 Relevance of ambient temperature on HDN process

A key physical parameter influencing HDN impact is the ambient temperature T_{a}. Lower T_{a} generally result in increased supersaturation levels, thereby enhancing HDN rates and amplifying the overall HDN impact. To investigate this dependence,

https://doi.org/10.5194/jecats-2026-16
Preprint. Discussion started: 25 August 2026

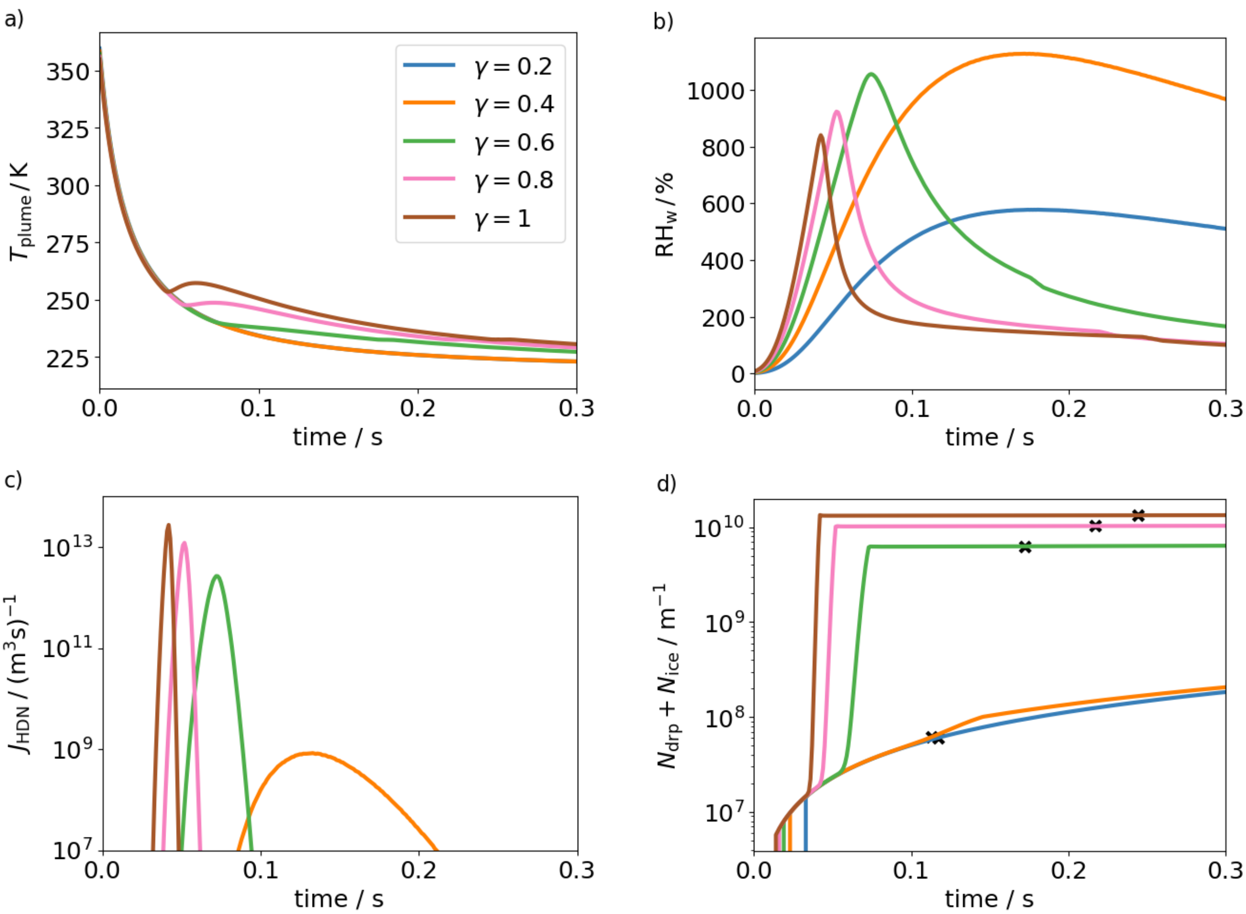

Figure 5. Temporal evolution of various quantities for the reference case.
a) Plume temperature, b) Relative humidity with respect to water, c) Nucleation rate J_{WS}, see Eq. (15), d) Sum of N_{drp} and N_{ice}. The crosses refer to the first time step for which droplets form into ice crystals.

T_a was systematically varied between $T_a = T_{ISA} - 20\,K$ and $T_a = T_{ISA}$. The resulting final ice crystal number $N_{ice,f}$ is presented in Fig. 6 as a function of the mixing line slope G, with distinct markers corresponding to different T_a. Marker colours denote the fraction of ice crystals formed via HDN, providing insight into the relative contribution of the different nucleation processes. G is linearly related to γ via Eq. (4) and is independent of T_a. Consequently, γ and G are interchangeable in this context, as indicated by the dual x-axis in Fig.6. The use of G offers a significant advantage in enabling comparative analysis across different propulsion systems. Consequently, in Fig. 6 gray and cyan shaded regions represent typical G values for kerosene- and hydrogen-fueled propulsion systems, respectively. Notably, G can be much larger for H_2FC aircraft than for aircraft with combustion engines. This effect is due to both a higher exhaust WV amount and lower exhaust temperatures for H_2FC aircraft. Assuming the same propulsion efficiency η, the G value for hydrogen combustion is equal to that of the FC case

https://doi.org/10.5194/jecats-2026-16
Preprint. Discussion started: 25 August 2026

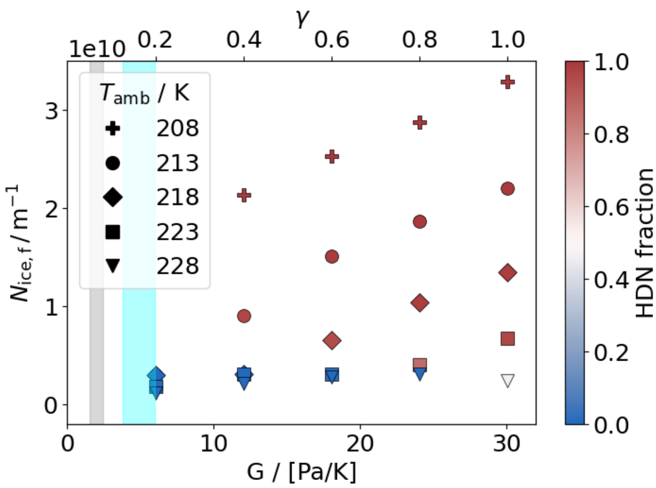

Figure 6. Final $N_{\mathrm{ice,f}}$ over the SAC mixing line slope G and γ, respectively. The colours represent the fraction of $N_{\mathrm{ice,f}}$ that were formed by HDN. The markers represent the different values for T_{a}. The gray area denotes typical value of G for kerosene combustion, while the cyan area denotes G values typical for hydrogen combustion.

when $\delta = \gamma = 0.2$.

Fig. 6 shows that the HDN fraction is either close to zero or approaches one, with a single exception in the lower-right region where the HDN contribution reaches approximately $50\,\%$. This indicates that HDN either plays a negligible role due to insufficient supersaturation in the plume, or dominates the ice formation process entirely. When HDN is active, it occurs rapidly and shortly after emission (see Fig. 5c). The resulting rapid depletion of supersaturation suppresses any subsequent activation of entrained aerosols and restricting droplet formation effectively to homogeneous nucleation.

Fig. 6 demonstrates the expected dependence: lower T_{a} result in higher supersaturation levels within the plume, thereby enhancing the nucleation rate of HDN and leading to increased $N_{\mathrm{ice,f}}$. This trend is consistently observed across all investigated WV levels in the exhaust. For the parameter range presented in Fig. 6, $N_{\mathrm{ice,f}}$ is higher when ice formation proceeds via HDN compared to nucleation on ambient aerosols. However, this conclusion may not hold under conditions of elevated ambient aerosol number concentrations, which will be addressed in the following section.

Notably, for $\gamma = 0.2$, HDN does not occur across the entire range of ambient temperatures considered. Fig. 6 reveals that decreasing the exhaust WV content, by reducing γ, results in a systematic reduction in $N_{\mathrm{ice,f}}$ for the same T_{a}. This highlights a viable technical pathway for mitigating contrail formation and their climate impact by actively reducing the WV emissions to avoid very high supersaturation values in the cooling plume.

4.4 Sensitivity analysis of HDN process

The HDN process exhibits strong non-linear behavior and high sensitivity to small perturbations in thermodynamic and microphysical conditions, as illustrated by the nucleation rate variations presented in Table 2. To assess the robustness of the

https://doi.org/10.5194/jecats-2026-16
Preprint. Discussion started: 25 August 2026

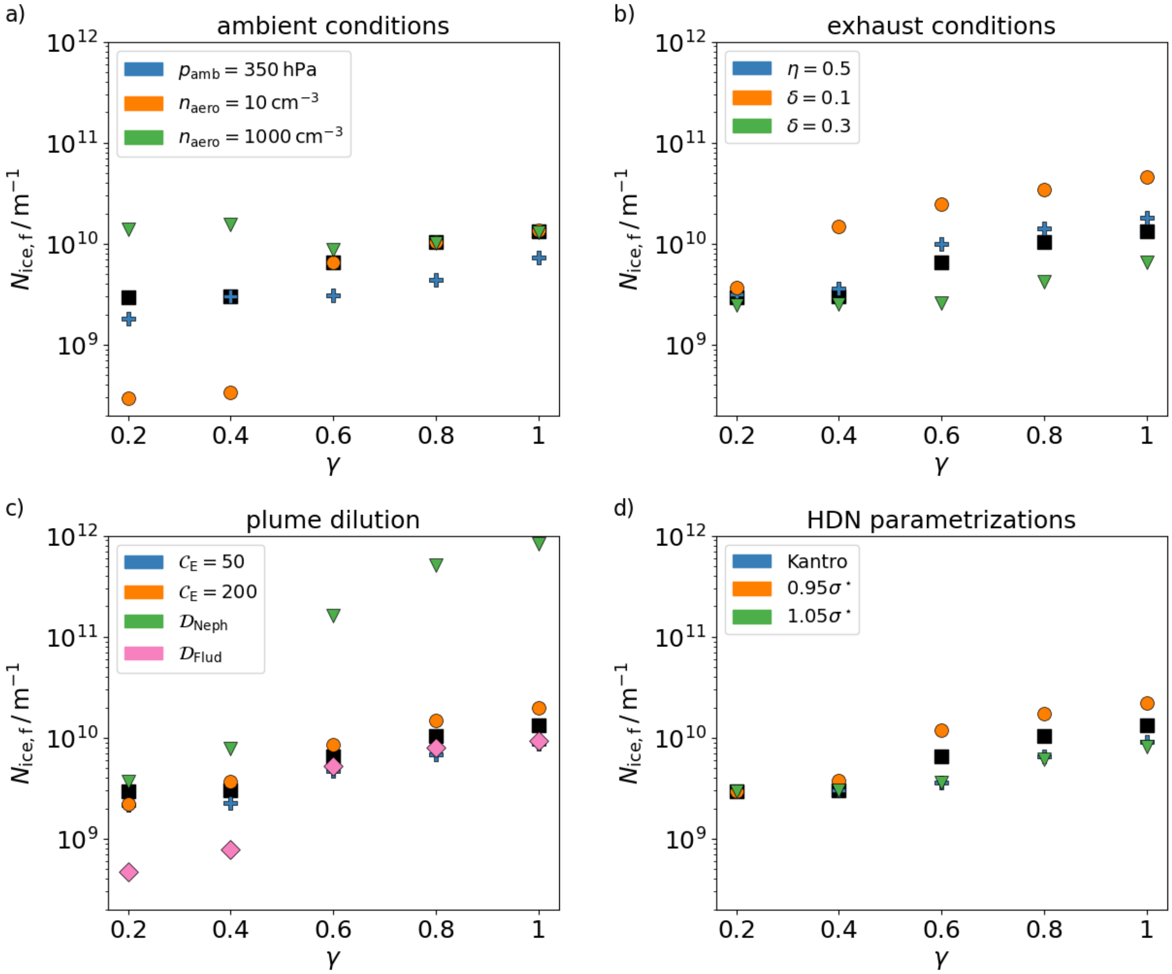

Figure 7. Sensitivity of $N_{\mathrm{ice,f}}$ along all γ values to a) ambient condition, b) exhaust properties conditions, c) plume dilution d) HDN parameterization. The black squares refer to the reference case. Each panel uses the same y-axis range.

https://doi.org/10.5194/jecats-2026-16
Preprint. Discussion started: 25 August 2026

simulation results and identify key drivers of uncertainty, a sensitivity analysis was conducted with respect to various parameters in the simulation setup. The list of varied parameters and their values are given in Table 4.

Fig. 7 shows the final ice crystal number $N_{\mathrm{ice,f}}$ for variations of individual parameters. The legend in each subplot indicates the value of the varied parameter. To enhance the interpretability, the analyzed parameters shown in each panel belong to a distinct category: ambient conditions, exhaust conditions, plume dilution and HDN parametrization. In all panels, black squares denote $N_{\mathrm{ice,f}}$ of the reference simulation. Fig. 7a illustrates the sensitivity to ambient pressure and number concentration of ambient aerosols. The dependence on ambient temperature T_{a} has already been shown in Fig. 6. Fig. 7a shows that an increased ambient pressure (without changing T_{a}) leads to a slight decrease of $N_{\mathrm{ice,f}}$ for all values of γ. For $\gamma \leq 0.4$, decreasing n_{aero} leads to slightly decreased $N_{\mathrm{ice,f}}$, while increasing n_{aero} leads to an increase in $N_{\mathrm{ice,f}}$. This dependence is less than linear, in line with the results in Zink et al. (2025a). For higher γ values, i.e. more initial WV in the exhaust, HDN occurs and ambient aerosol activation is suppressed, rendering $N_{\mathrm{ice,f}}$ independent from n_{aero}.

Fig. 7b illustrates the sensitivity of $N_{\mathrm{ice,f}}$ to variations in exhaust conditions. An increase in the overall propulsion efficiency η results in a modest enhancement of $N_{\mathrm{ice,f}}$. The relative heat emission factor δ exhibits a more pronounced influence for cases, where HDN is triggered. Decreasing δ leads to an increase in $N_{\mathrm{ice,f}}$, whereas increasing δ reduces $N_{\mathrm{ice,f}}$, with changes of a factor of approximately 3. In contrast, $N_{\mathrm{ice,f}}$ shows significantly reduced sensitivity to δ in the absence of HDN. Furthermore, for an increase in δ the onset of HDN is reduced to $\gamma \geq 0.8$, while a reduction in δ promotes earlier HDN onset at lower $\gamma \geq 0.4$.

Fig. 7c presents the impact of initial dilution, characterized by the air-to-fuel ratio $\mathcal{C}_{\mathrm{E}}$ and the dilution rate $\mathcal{D}(t)$ on $N_{\mathrm{ice,f}}$. The air-to-fuel ratio of the exhaust $\mathcal{C}_{\mathrm{E}}$ governs the initial thermodynamic state of the exhaust plume, directly affecting its temperature and humidity via Eqs. (2) and (1), influencing the exhaust density and thereby the exhaust mass flow $\dot{m}_{\mathrm{E}}$ according to Eq. (7). Varying $\mathcal{C}_{\mathrm{E}}$ shifts the initial conditions along the mixing line, thereby altering the timing at which the plume reaches supersaturation thresholds required for HDN. This shift modifies both the plume area and the dilution rate at the onset of HDN, thereby affecting the number of droplets formed. Fig. 7c indicates that increasing $\mathcal{C}_{\mathrm{E}}$ leads to a slight increase in $N_{\mathrm{ice,f}}$ if HDN is triggered, while a decrease in $\mathcal{C}_{\mathrm{E}}$ results in a small reduction in $N_{\mathrm{ice,f}}$. A decreased $\mathcal{C}_{\mathrm{E}}$ leads to an earlier onset of HDN and thus a smaller plume area, reducing the number of droplets formed by HDN. Different dilution rates change $N_{\mathrm{ice,f}}$ by up to one order of magnitude for low values of $\gamma \leq 0.4$. The lower $N_{\mathrm{ice,f}}$ observed for the weaker dilution $\mathcal{D}_{\mathrm{Flud}}$ arises from more efficient WV depletion during plume expansion, which limits the activation of entrained aerosols into liquid droplets and, consequently, reduces the number of ice crystals. In contrast, the stronger dilution $\mathcal{D}_{\mathrm{Neph}}$ results in less effective vapour depletion, allowing a greater fraction of aerosols to activate and contribute to ice formation. For $\gamma \geq 0.6$, the influence of dilution rate becomes increasingly pronounced, as HDN dominates the ice formation process. Faster dilution leads to higher $\mathrm{RH}_{\mathrm{w,max}}$, as more droplets must form via HDN to produce enough latent heat to overcome the temperature decrease by dilution. For $\gamma = 1$, the difference in $N_{\mathrm{ice,f}}$ between strong and weak dilution reaches nearly two orders of magnitude, underscoring the critical role of dilution dynamics for the HDN impact.

Fig. 7d focuses on parameters that directly change the calculation of the HDN rate. Here, $N_{\mathrm{ice,f}}$ is shown if the nucleation rate J_{Kan}, Eq. (14), is used instead of J_{WS}, Eq. (15). Additionally, the surface tension σ of nucleated droplets is varied by $5\,\%$ con-

https://doi.org/10.5194/jecats-2026-16
Preprint. Discussion started: 25 August 2026

sistent with the uncertainty range reported in Starzmann et al. (2018). A reduction in σ increases $N_{\mathrm{ice,f}}$ by up to a factor of 2, while both the use of J_{Kantro} and a decreased σ lead to reductions in $N_{\mathrm{ice,f}}$ of less than a factor of 2. The physical accuracy of either nucleation rate parametrization remains uncertain, as no experimental data are currently available for the thermodynamic conditions typical of moist aircraft exhaust plumes. Consequently, the choice of HDN rate formulation introduces an inherent uncertainty of approximately a factor of 2 in the predicted $N_{\mathrm{ice,f}}$, both upward and downward.

Hence, if the exhaust is moist enough to trigger HDN, the number of formed ice crystals is most sensitive to the dilution rate $\mathcal{D}(t)$. Stronger dilution lead to a strong increase of $N_{\mathrm{ice,f}}$, while a slower dilution reduces $N_{\mathrm{ice,f}}$ only slightly.

5 Discussion

5.1 Strengths and limitations of the current model

In a previous study (Hillenbrand and Unterstrasser, 2026), it was demonstrated that thermodynamic plume conditions within plumes behind H_2FC aircraft can trigger droplet formation via HDN. The analysis in that study was based on the mixing curve theory, a thermodynamic framework that neglects microphysical processes. As a result, utilized in Hillenbrand and Unterstrasser (2026), inherently overestimates the supersaturation reached during plume dilution, potentially over-exaggerating the potential relevance of HDN on contrail formation. Therefore, the HDN process has been incorporated into the LCM box model, enabling a systematic and physically consistent investigation of HDN in very moist aircraft plumes. The present study presents the first assessment of the HDN relevance impact on contrail formation behind H_2FC aircraft. Although homogeneous nucleation has been previously examined in the context of aerodynamic contrail formation (Jansen and Heymsfield, 2015), the underlying physical mechanisms differ significantly.

The implementation of HDN within the LCM box model has been validated against state-of-the-art fluid-dynamic simulations using nozzle test cases, as demonstrated in Sec. 3.2. The validation shows that the LCM box model exhibits high predictive accuracy, even though dynamical effects such as turbulence are not explicitly simulated. This indicates that, especially for cases where HDN occurs, microphysical processes dominate over dynamical effects. However, the extent to which this conclusion applies to plumes generated by H_2FC aircraft remains uncertain, as no experimental nor numerical data exist to validate HDN-driven contrail formation. Furthermore, the assumption of a spatially homogeneous plume represents a significant simplification that may influence the simulation outcome. In reality, the plume is inherently heterogeneous, with spatial variations in temperature and humidity. A multi-trajectory approach or radially-resolving model, as proposed in Lottermoser and Unterstrasser (2024) would capture these conditions more realistically. As the HDN rate is highly sensitive to thermodynamical conditions, it is uncertain whether these effects can be averaged by a mean trajectory as in the case of kerosene combustion (Bier et al., 2022). While multi-trajectory approaches have been applied to conventional turbine exhausts (e.g. (Vancassel et al., 2014)), their applicability to H_2FC aircraft is unsuitable for direct adaptation due to fundamental differences in plume characteristics. Currently, CFD data for diluting H_2FC aircraft plumes have only been analysed in terms of mean plume properties, precluding a detailed assessment of spatial heterogeneity.

Despite the simplifying assumption of a homogeneous plume, this study provides critical first insights into the potential role

https://doi.org/10.5194/jecats-2026-16
Preprint. Discussion started: 25 August 2026

of HDN in very moist aircraft plumes. First, microphysical simulations confirm that HDN is indeed feasible under very moist exhaust conditions of H_2FC aircraft exhausts. If HDN occurs, it happens almost immediately after emission, requiring a substantially refined temporal resolution of contrail formation processes. HDN occurrence effectively suppresses heterogeneous ice nucleation on ambient aerosols, making final ice crystal numbers largely independent of the ambient aerosol number concentration. Despite this suppression, HDN leads to an increase in $N_{\mathrm{ice,f}}$ compared to scenarios where ice forms exclusively on entrained aerosols. However, this enhancement is more moderate than previously anticipated by Hillenbrand and Unterstrasser (2026). The maximum relative humidity values given in their Fig. 6 suggest significantly higher nucleation rates than observed in this study. These high relative humidity values are not attained in microphysical simulations due to the rapid depletion of supersaturation through early droplet formation via HDN, as shown in Fig. 5b.

5.2 Comparison with contrails behind combustion aircraft

FC technology is expected to be implemented in regional aircraft, flying at low altitude. There, ambient temperatures are generally higher than those encountered during long-haul aircraft missions. For ambient temperature values $T_\mathrm{a} \geq 230\,\mathrm{K}$, the supersaturation values within the plume are too low to trigger HDN (see Fig. 6), and ice crystals can only form by ambient aerosol activation. Additionally, ice crystal formation can then be limited by the homogeneous freezing temperature of water droplets. This effect has been shown with comparison of in-situ measurement data and LCM box model simulations behind a prototype fuel cell exhaust emulator (Braun et al. (2026).

In Lottermoser and Unterstrasser (2026), the initial ice crystal number, representing a contrail from kerosene combustion with a typical soot number emission index, was scaled both up and down to account for different scenarios. Their reference value for kerosene combustion has been chosen to be $N_{\mathrm{ice,kero}} = 10^{12}\,\mathrm{m}^{-1}$. The down-scaling (by factors 10 and 100) represents ice crystal formation exclusively on entrained aerosols, while the up-scaling (by factors 10 and 100) was included to account for possibly very high HDN rates for H_2FC aircraft, or for nucleation on volatile particles or lubrication oil for hydrogen combustion. Our results show that, under realistic plume conditions for a H_2FC aircraft, having a higher initial number of ice crystals than in a kerosene combustion case is physically not plausible. The maximum $N_{\mathrm{ice,f}}$ for H_2FC aircraft calculated in our simulations has been found for the strongest dilution $\mathcal{D}_{\mathrm{Neph}}$ and is of the same order of magnitude as the reference values used in Lottermoser and Unterstrasser (2026).

Comparing $N_{\mathrm{ice,f}}$ for individual contrails for different propelled aircraft is not straightforward. For hydrogen combustion $N_{\mathrm{ice,f}}$ depends heavily on oil emissions and whether oil droplets can serve as condensation nuclei for droplet formation (Zink et al., 2025b; Ponsonby et al., 2024). For kerosene combustion $N_{\mathrm{ice,f}}$ mainly depends on the number of soot particles emitted (Bier et al., 2022), but is also influenced by volatile particle emissions (Yu et al., 2024). The limiting temperature below which a contrail forms is lower for kerosene combustion than for hydrogen usage. Let's assume a kerosene propelled aircraft with the same propulsion parameters than the reference case, without reducing heat or WV from the exhaust, flying at the same altitude. For this aircraft, the resulting limiting temperature is $T_{\mathrm{lim}} \approx 228\,\mathrm{K}$, which is approximately T_{ISA} at the given flight level. Therefore, for the reference case temperature ($T_{\mathrm{ISA}} - 10\,\mathrm{K}$), a kerosene propelled aircraft would also form a contrail.

Experimental and numerical investigations of contrail formation behind kerosene-fueled aircraft indicate that the apparent ice

https://doi.org/10.5194/jecats-2026-16
Preprint. Discussion started: 25 August 2026

emission index are on the order of $\mathrm{AEI_{ice}} \approx 10^{14} - 10^{16}$ per kilogram fuel burnt (Yu et al., 2024; Voigt et al., 2026; Neumann et al., 2025). From our simulations, $\mathrm{AEI_{ice}}$ can be estimated using

$$\mathrm{AEI_{ice}} = \frac{\mathrm{N_{ice,f}}}{\hat{\mathrm{m}}_{\mathrm{H_2}}} = \frac{2.79\,\mathrm{N_{ice,f}}}{\hat{\mathrm{m}}_{\mathrm{kero,\,equiv}}} \tag{19}$$

where $\hat{m}_{\mathrm{H_2}}$ is the fuel consumption of hydrogen per unit flight distance, while $\hat{m}_{\mathrm{kero,\,equiv}} = 2.79\,\hat{m}_{\mathrm{H_2}}$ denotes the energy-equivalent fuel consumption in terms of kerosene due to the higher combustion value Q of hydrogen.

Due to the strong dependence of $\hat{m}_{\mathrm{H_2}}$ on aircraft design, precise values for future H_2FC aircraft remain uncertain and must be estimated based on available reference data. The DLR EXACT project (Atanasov and Silberhorn, 2025) provides an estimated hydrogen consumption of $\hat{m}_{\mathrm{H_2}} \approx 0.3\,\mathrm{g/m}$, corresponding to the hydrogen mass flow rate $\dot{m}_{\mathrm{H_2}}$ specified in Table 4 and $\hat{m}_{\mathrm{kero,\,equiv}} \approx 0.84\,\mathrm{g/m}$.

Applying Eq. (19) leads to $\mathrm{AEI_{ice,\,equiv}} \approx 10^{13}\,\mathrm{kg^{-1}\,H_2}$ for the reference case. For the scenario with the strongest dilution $\mathcal{D}_{\mathrm{Neph}}$, leading to the maximum ice crystal number, $\mathrm{AEI_{ice}}$ reaches approximately $10^{15}\,\mathrm{kg^{-1}\,H_2}$. Thus, the estimated $\mathrm{AEI_{ice}}$ for the worst case scenario for H_2FC aircraft is comparable to the observed range for kerosene-fueled aircraft. However, it should be noted, that $\mathrm{AEI_{ice}}$ values for kerosene propulsion are primarily derived from large-scale aircraft, while the results in the present study apply for a regional aircraft. Consequently, direct comparisons between the two propulsion systems remain limited by differences in aircraft size.

5.3 Contrail formation reduction options

We find that the number of formed ice crystals is highly variable depending mainly on exhaust properties, ambient temperature and dilution rate. The dilution rate is crucial during the first second after emission as HDN occurs within this time range. Stronger dilution enhances the potential for HDN by limiting the efficiency of supersaturation depletion, thereby allowing for higher peak relative humidity levels.

The dilution rate of current turbo-jet aircraft can be related to the evolution of a free jet, rendering the scaling laws of these flow dynamics applicable. This is not straightforward for H_2FC aircraft. The exhaust velocity for a H_2FC aircraft is expected to be much slower as the thrust of the exhaust is not used for moving the aircraft. This can lead to a 'negative jet' in a reference frame that is moving with the aircraft. Additionally, propeller-induced motion enhances the mixing of air masses downstream, potentially enhancing the dilution. The angular velocities induced by this motion also differ from a classical view of a free jet. The position of the FC exhaust can also influence the dilution of the plume. If the exhaust stream is emitted close to the aircraft frame, the plume could be confined within the aircraft's boundary layer. Within this region, turbulent mixing is reduced and the exhaust cannot evolve as a free jet, thereby reducing the dilution rate during the initial phase of emission. The combination of all those effects make a general prediction of the dilution rate for H_2FC aircraft uncertain. Estimates of the dilution rate derived from dedicated CFD simulations for H_2FC exhaust plumes and extrapolated from in-situ measurements (Braun et al., 2026) differ by a factor of 10 during the first second after emission, when HDN can occur. This discrepancy translates into a potential two order of magnitude variation in simulated $N_{\mathrm{ice,f}}$ underscoring the high sensitivity of HDN outcomes to the assumed mixing

https://doi.org/10.5194/jecats-2026-16
Preprint. Discussion started: 25 August 2026

dynamics. The dilution rate is strongly governed by the exhaust jet characteristics such as velocity, temperature, and mass flow rate. Therefore, the dilution data used in this study to describe the exhaust evolution may not be representative for future H_2FC aircraft. Additionally, strategic design of the exhaust plume flow can help to decrease the number of ice crystals behind H_2FC aircraft. The dilution is expected to be weaker if the exhaust is not placed directly behind the propellers and if it can be contained within the boundary layer of the aircraft frame.

Beyond the dilution rate, ambient conditions, especially the ambient temperature, play a decisive role in determining the significance of HDN. At lower T_a, the thermodynamic conditions favour higher supersaturation levels resulting in a more pronounced HDN impact. Consequently, HDN is primarily relevant under cold atmospheric conditions ($T_\mathrm{a} \lessapprox 213\,\mathrm{K}$), which are less frequent for low flight altitudes. In contrast, persistent contrail formation is restricted to ISSRs, which are generally colder than the surrounding atmosphere. The occurrence frequency of ISSRs has been extensively documented for high-altitude flight regimes, where most conventional jet aircraft operate. However, this limits our understanding of ISSR prevalence at lower altitudes, where future H_2FC regional aircraft are expected to operate. Therefore, a systematic investigation on ISSR occurrence at lower flight altitudes is necessary for accurately evaluating the climate impact of contrail formation in the context of future H_2FC regional aircraft.

This study demonstrates that reducing the WV content in the exhaust of H_2FC aircraft directly suppresses the HDN process, thereby reducing $N_\mathrm{ice,f}$. As a rough practical guideline derived from our simulations, the slope of the mixing line, calculated by Eq. (4), should be kept below $G < 10\,\mathrm{Pa/K}$ to mitigate a non-linear increase of $N_\mathrm{ice,f}$ due to HDN. This threshold represents a critical design criterion for minimizing contrail formation potential in H_2FC aircraft. To achieve this reduction (Hillenbrand and Unterstrasser, 2026) proposed to integrate water vapour condensers into the propulsion system, see Fig. 1. These devices could condense WV from the exhaust stream prior to emission, producing liquid water. The condensed WV could be released as liquid droplets at a position where they can not re-moisturize the contrail forming exhaust. By doing so, the remaining WV available for nucleation would be reduced, potentially leading to a net decrease in the number of droplets formed via HDN. However, such a system would introduce additional mass and require electrical power, thereby potentially reducing propulsion efficiency. Given that contrail formation only exerts a climate impact when aircraft fly through ISSRs, the use of condensers could be limited to these flight phases. Additionally, the maximum capacity for WV condensation remains uncertain. To account for this uncertainty, the WV emission factor is systematically varied from $\gamma = 1$ (no reduction) to $\gamma = 0.2$ ($80\,\%$ reduction). While the technical feasibility, system integration, and energy trade-offs of such condensation systems remain to be evaluated in future engineering studies, our findings suggest that they are a promising opportunity for actively mitigating contrail formation for future H_2FC aircraft.

6 Conclusions

This study investigates the influence of Homogeneous Droplet Nucleation (HDN) on the ice crystal number formed in exhaust plumes behind H_2FC aircraft. The HDN process is implemented within the LCM box model, a model for contrail formation simulations, previously applied in kerosene and hydrogen combustion scenarios. A rigorous numerical validation is performed,

https://doi.org/10.5194/jecats-2026-16
Preprint. Discussion started: 25 August 2026

including temporal convergence assessments for cases exhibiting the highest nucleation rates. Additionally, a comparison against various simulation codes used for steam turbine applications is performed via two nozzle benchmark test cases. The box model results lie within the range of the CFD codes demonstrating accurate implementation of the HDN process.

This study presents the first comprehensive analysis of the role of HDN in exhaust plumes from future H_2FC aircraft. A reference scenario representative of PEM-FC propulsion, characterized by low exhaust temperatures, was adopted to explore the plume's microphysical evolution under realistic flight conditions. The low temperature of the exhaust leads to high supersaturation levels during dilution, creating favourable conditions for high HDN rates. To assess the potential of mitigation strategies, the impact of varying degrees of exhaust WV reduction was investigated. Given the highly non-linear dependence of HDN on thermodynamic conditions, a sensitivity analysis was conducted, regarding numerical implementation and aircraft design choices.

The occurrence and impact of HDN depend on various parameters, especially the exhaust and ambient temperature, the exhaust WV content and the dilution rate of the plume. Under cold ambient conditions and in the absence of significant WV reduction, HDN leads to an enhanced formation of ice crystals compared to nucleation on ambient aerosols. While this enhancement typically results in a moderate increase, less than one order of magnitude, it can be amplified under extreme conditions, such as very rapid dilution and low ambient temperatures. However, contrary to predictions from purely thermodynamic studies that suggest increases in ice crystal number of several orders of magnitude, our results indicate a more moderate effect, even when HDN occurs. As a result, future H_2FC aircraft with adequate design measures to minimize HDN occurrence are expected to produce fewer ice crystals compared to a future Kerosene/SAF turbo-prop aircraft.

The installation of onboard water vapour condensers to reduce exhaust moisture content offers a possible pathway to suppress HDN, thereby restricting ice formation to ambient aerosol nucleation. Such a strategy could lead to a further reduction in ice crystal numbers. Therefore, we encourage future research into the technical feasibility, efficiency, and integration of water condensation systems. As a preliminary design guideline, we propose that the mixing line slope, that can be calculated by Eq. (4), should roughly be $G \lessapprox 10$ Pa/K to minimize the likelihood of HDN occurence. This rule-of-thumb criterion is based on contrail formation simulation with several idealizing assumption and the exact value may change. Yet, it should raise awareness that adaptation of FC emissions is key to contrail mitigation and can guide the design process of a FC aircraft towards small contrail climate impact.

The design of future H_2FC aircraft remains uncertain leading to significant uncertainty in key parameters that govern ice crystal formation. While this study has incorporated selected parameter sensitivities to assess their influence on HDN and ice crystal numbers, a systematic exploration of the parameter space remains open. A comprehensive parameter study is therefore the next step to develop a robust parametrization of ice crystal number to clarify the relative importance of HDN across different FC aircraft configurations. Furthermore, a direct comparison between the mean trajectory approach adopted here and more advanced modeling strategies accounting for radial heterogeneity within the plume is essential. This would enable an assessment of the validity and limitations of the mean trajectory assumption, particularly under conditions where plume inhomogeneity may influence nucleation processes.

https://doi.org/10.5194/jecats-2026-16
Preprint. Discussion started: 25 August 2026

Appendix A: Dilution data

The LCM box model requires as input the temporal evolution of the aircraft exhaust plume, specifically its dilution dynamics. This dilution evolution can be derived from three-dimensional computational fluid dynamics (CFD) simulations of the plume behind a representative aircraft configuration. The plume cross-sectional area can either be resolved via an ensemble of individual trajectory samples or represented by a mean-state description. In both approaches, the dilution rate is subsequently computed from the temporal evolution of temperature within the plume, following the formulation presented in Eq. (17) of Bier et al. (2022):

$$\mathcal{D}(t) = \frac{T(t) - T_\mathrm{a}}{T_\mathrm{E} - T_\mathrm{a}} \tag{A1}$$

In this study, different dilution evolution scenarios are employed to characterize the plume dynamics. The reference case dilution $\mathcal{D}$ is based on a dedicated CFD simulation conducted for a H_2FC aircraft under conditions closely matching those specified in Table 4.

The CFD simulation results were analyzed across multiple cross-sectional planes downstream of the aircraft exhaust outlet. For each cross section, the plume boundary was defined by all computational cells in which the mass fraction of WV exceeded a predefined threshold value $\chi_{\mathrm{wv,min}} = 10^{-4}$. Analysis of the results confirmed that all identified plume cross sections exhibited smooth, connected structures without discontinuities originating from numerical fluctuations.

In the absence of individual particle trajectory data from the CFD simulation, a simplified modeling approach was adopted in which each plume cross section is represented by a single mean trajectory. The mean temperature within each cross section has been calculated by a cell-volume weighted mean over all cells representing the plume area. This approach, which assumes a representative dilution path for the plume, was previously evaluated against a full ensemble of stochastic trajectories in Bier et al. (2022) for kerosene-powered aircraft. They found that, for kerosene combustion, the resulting ice crystal numbers of both approaches were comparable, while the mean trajectory simulation is much faster than the multiple trajectory approach. We weighted the gain in computation time more important than the loss of accuracy for a first analysis of contrail formation behind fuel cell propelled aircraft.

Accordingly, the plume area in each cross section is employed to calculate the mean velocity and temperature of the plume. The dilution factor in each cross section has been calculated using the mean temperature $\bar{T}_i$ by

$$\mathcal{D}_i = \frac{\bar{T}_i - T_a}{T_\mathrm{E} - T_a} \tag{A2}$$

To ensure a continuous decrease in $\mathcal{D}_i$, a least-square fit to a power law with logarithmic weighted errors is utilized, as this approach enables an accurate approximation even for minimal dilution values. The evolution of the inverse dilution factor is shown in Fig. A1 in blue.

The other dilution rates used for investigation of the sensitivity of HDN are given in Table 4. The dilution $\mathcal{D}_{\mathrm{Flud}}$ has been

https://doi.org/10.5194/jecats-2026-16
Preprint. Discussion started: 25 August 2026

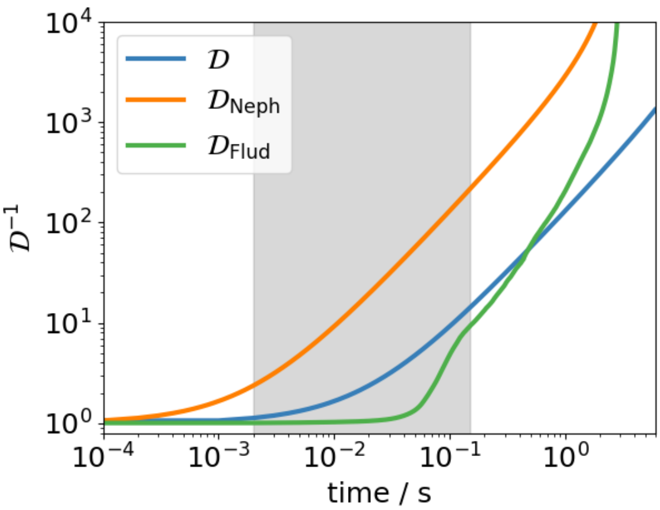

Figure A1. Inverse dilution factor for mean trajectories derived from different data sources. The gray area indicates the time where the HDN process can become relevant.

originally presented in Vancassel et al. (2014) and describes the plume dilution behind an CFM56 engine nozzle of an A340-300 aircraft. The original data contains 25.000 trajectories and has been reduced to a mean trajectory in Bier et al. (2022). The dilution $\mathcal{D}_{\mathrm{Neph}}$ is the extension of measured in-situ data behind an exhaust emulating potential exhaust conditions for H_2FC aircraft (Braun et al., 2026). The in-flight data has been measured with a dilution tracer at distances of more than $50\,\mathrm{m}$ and a power law has been fitted to the data and extrapolated towards the exhaust plane. It should be noted that this dilution evolution may not be representative of future H_2FC aircraft, particularly shortly after emission, owing to the potentially differing location and design of the emulator.

The comparison of the inverse dilution rates is shown in Fig. A1. The gray area denotes the time where the HDN process can be triggered and the dilution rate is especially important. Focusing on the gray area, it can be seen that the reference case dilution $\mathcal{D}$ lies in between the fast dilution $\mathcal{D}_{\mathrm{Neph}}$ and the slow dilution $\mathcal{D}_{\mathrm{Flud}}$.

Appendix B: Microphysics of small particles

Initially, pure water droplets created by HDN can be orders of magnitude smaller than water droplets formed on solid nuclei (Jansen and Heymsfield, 2015). Therefore, we verify that the formulas implemented in the LCM box model are also applicable to describe the behavior of these very small droplets.

The mathematical description of the behavior of small particles is split into two distinct regimes: the free molecular regime and the continuum regime. The non-dimensional Knudsen number is used to distinguish between the two regimes:

https://doi.org/10.5194/jecats-2026-16
Preprint. Discussion started: 25 August 2026

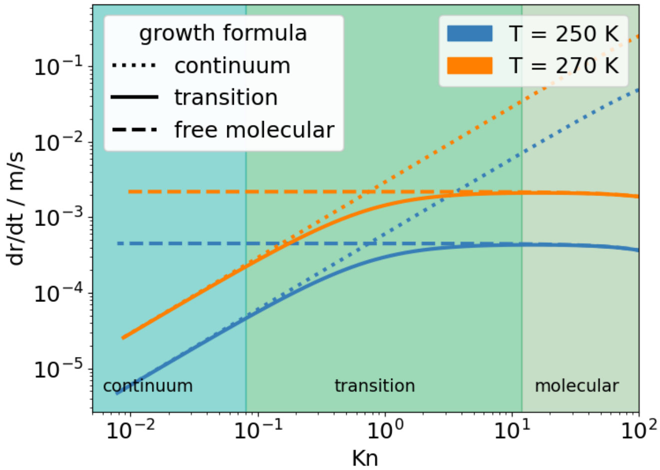

Figure B1. Radial growth rate over the Knudsen number for the different condensational growth regimes: the continuum regime, the transition regime and the free molecular regime. All formulas are applied for a constant relative humidity value $\mathrm{RH_w} = 500\,\%$ and two distinct temperature values $T = \{250, 270\}$ K. The transition formulation is implemented in the box model and accurately covers the growth for all droplet sizes.

$$\mathrm{Kn} = \frac{\lambda_\mathrm{free}}{\mathrm{r_p}} \qquad \text{with } \lambda_\mathrm{free} = \frac{2\mathrm{D_i}}{\sqrt{2\mathrm{R_i T}}} \tag{B1}$$

760 λ_free represents the mean molecular free path length and r_p is the radius of the particle, while D_i and R_i are the diffusion coefficient and specific gas constant of the vapour. For typical conditions in supersaturated aircraft plumes, i.e. $T < 0$°C and low air pressure, $\lambda_\mathrm{free} \approx 10^{-7}\,\mathrm{m}$ for WV in air. If $\mathrm{Kn} \ll 1$, the particle is large compared to the mean free path length and can be treated as a continuum, for which macroscopic laws apply. Conversely, for $\mathrm{Kn} \gg 1$ the particle is considered to be in the free molecular regime and kinetic gas theory must be employed to describe the physical processes affecting the particle.

765 Seinfeld and Pandis (1998) present the molar growth rate for both the molecular and the continuum regime. The molar growth rate $\mathrm{d}n/\mathrm{d}t$ for droplets in the continuum regime can be calculated by their Eq. (12.12):

$$\left(\frac{\mathrm{dn}}{\mathrm{dt}}\right)_\mathrm{conti} = 4\pi r_p D\left(c_\infty - c_\mathrm{s}\right) \tag{B2}$$

where D is the diffusivity of WV in air, c_∞ is the WV concentration in the ambient environment and c_s is the vapour-phase concentration at the particle surface.

770 For droplets in the free molecular regime the molar growth rate is given by their Eq. (12.25):

$$\left(\frac{\mathrm{dn}}{\mathrm{dt}}\right)_\mathrm{molec} = \pi r_\mathrm{p}^2 \bar{u}\beta\left(c_\infty - c_\mathrm{s}\right), \tag{B3}$$

where $\bar{u} = \sqrt{8R_\mathrm{wv}T/\pi}$ is the mean velocity, R_wv is the gas constant of WV and β is the molecular accommodation coefficient. The regime between the continuum and free molecular regime, where $r_\mathrm{p} \approx \lambda_\mathrm{free}$, is called transition regime. Among others,

https://doi.org/10.5194/jecats-2026-16
Preprint. Discussion started: 25 August 2026

Fuchs and Sutugin (1971) proposed a solution how to smoothly combine the equations governing diffusional growth in the molecular regime with the equations applicable in the continuum regime. They introduced a transition factor depending solely on the Knudsen number of the particle:

$$\left(\frac{\mathrm{dn}}{\mathrm{dt}}\right)_{\mathrm{trans}} = \left(\frac{\mathrm{dn}}{\mathrm{dt}}\right)_{\mathrm{conti}} \frac{1+\mathrm{Kn}}{1+1.71\mathrm{Kn}+1.33\mathrm{Kn}^2} \tag{B4}$$

This formula for condensational growth is implemented in the LCM box model and has been used in previous publications (Bier et al., 2022; Zink et al., 2025b). The radial growth rates $\mathrm{d}r/\mathrm{d}t$ of water droplets in a supersaturated environment are shown in Fig. B1 over a large range of Knudsen numbers. We choose an exemplary relative humidity value of $\mathrm{RH_w} = 500\,\%$ and two distinct temperature values $T = \{250, 270\}$ K as environmental gas conditions. The shaded areas correspond to the distinct growth regimes. The continuum formula holds only for small values of Kn, corresponding to large particles. In contrast, the molecular formula is only applicable for large Kn, i.e. small particles. The transition formula fits the growth laws in both regimes and approximates the condensational growth accurately over the whole range of Knudsen numbers. The existing depositional growth rates for ice crystals in the LCM box model, as given in Eq. (7) of Bier et al. (2022), include similar transitional correction factors. In summary, we can conclude that the equations implemented in the LCM box model are capable of accurately describing the behavior of small droplets and ice crystals.

Code and data availability. All simulation data have been created with the Lagrangian Cloud Module (LCM) in a box model approach, described in Sec. 2. The simulation results, together with the plot script required to reproduce the figures in this study, are available via a Zenodo repository (Hillenbrand, 2026).

Author contributions. DH and SU developed the code and chose the simulation setups. DH performed the simulations and analysed the results. DH and SU wrote manuscript.

Competing interests. At least one of the authors is a member of the editorial board of Journal of Environmentally Compatible Air Transport System.

Acknowledgements. This work has been funded by the DLR internal projects H2EAT and H2CONTRAIL. Both authors received funding from Airbus SAS within the framework of understanding contrails from hydrogen propulsion. ChatAI (GWDG) was used to assist with manuscript editing.
We thank Sebastian Schuster (ORCID-ID: 0000-0002-2055-1163) for providing the data from Starzmann et al. (2018) and his help with their analysis. We thank the aerodynamic department of Airbus for providing the CFD data, the dilution calculation is based on. We thank

https://doi.org/10.5194/jecats-2026-16
Preprint. Discussion started: 25 August 2026

Charles Renard and Florian Thorey (both Airbus Operations SAS, Toulouse, France) for their collaboration. We thank Charles Renard for an independent review and Simon Kirschler (ORCID-ID: 0000-0003-4232-8277) for an internal review of the paper draft.

https://doi.org/10.5194/jecats-2026-16
Preprint. Discussion started: 25 August 2026

References

Adler, E. J. and Martins, J. R.: Hydrogen-powered aircraft: Fundamental concepts, key technologies, and environmental impacts, Prog. Aerosp. Sci., 141, 100 922, https://doi.org/10.1016/j.paerosci.2023.100922, special Issue on Green Aviation, 2023.

Ansell, P. J.: Review of sustainable energy carriers for aviation: Benefits, challenges, and future viability, Prog. Aerosp. Sci., 141, 100 919, https://doi.org/10.1016/j.paerosci.2023.100919, 2023.

Atanasov, G. and Silberhorn, D.: EXACT Sustainable Aircraft Concepts Results and Comparison, DLRK 2024, https://doi.org/10.25967/630388, 2025.

Aviation Benefits, 2024: Aviation: Benefits Beyond Borders 2024, https://aviationbenefits.org/downloads/aviation-benefits-beyond-borders-2024, accessed: 2026-05-11, 2024.

Bakhtar, F., Young, J. B., White, A. J., and Simpson, D. A.: Classical Nucleation Theory and Its Application to Condensing Steam Flow Calculations, Proceedings of the Institution of Mechanical Engineers, Part C: Journal of Mechanical Engineering Science, 219, 1315–1333, https://doi.org/10.1243/095440605X8379, 2005.

Baroutaji, A., Wilberforce, T., Ramadan, M., and Olabi, A. G.: Comprehensive investigation on hydrogen and fuel cell technology in the aviation and aerospace sectors, Renewable and Sustainable Energy Reviews, 106, 31–40, https://doi.org/10.1016/j.rser.2019.02.022, 2019.

Becker, R. and Döring, W.: Kinetische Behandlung der Keimbildung in übersättigten Dämpfen, Annalen der Physik, 416, 719–752, https://doi.org/https://doi.org/10.1002/andp.19354160806, 1935.

Bier, A., Unterstrasser, S., and Vancassel, X.: Box model trajectory studies of contrail formation using a particle-based cloud microphysics scheme, Atmos. Chem. Phys., 22, 823–845, https://doi.org/10.5194/acp-22-823-2022, 2022.

Bier, A., Unterstrasser, S., Zink, J., Hillenbrand, D., Jurkat-Witschas, T., and Lottermoser, A.: Contrail formation on ambient aerosol particles for aircraft with hydrogen combustion: a box model trajectory study, Atmos. Chem. Phys., 24, 2319–2344, https://doi.org/10.5194/acp-24-2319-2024, 2024.

Braun, S., Pühl, M., Marsing, A., Sauer, D., Neumann, G., de la Torre Castro, E., Hahn, V., Lichtenstern, M., Stock, P., Heckl, C., Hillenbrand, D., Roiger, A., Voigt, C., Unterstraßer, S., Vasenden, A., Vasenden, R., Cammas, J., Thorey, F., Mackay, C., Renard, C., and Jurkat-Witschas, T.: Towards quantifying contrails of fuel cell powered aircraft: first in-flight measurements of a fuel cell exhaust emulator, EGUsphere, 2026, 1–36, https://doi.org/10.5194/egusphere-2026-2887, 2026.

Brock, C. A., Froyd, K. D., Dollner, M., Williamson, C. J., Schill, G., Murphy, D. M., Wagner, N. J., Kupc, A., Jimenez, J. L., Campuzano-Jost, P., Nault, B. A., Schroder, J. C., Day, D. A., Price, D. J., Weinzierl, B., Schwarz, J. P., Katich, J. M., Wang, S., Zeng, L., Weber, R., Dibb, J., Scheuer, E., Diskin, G. S., DiGangi, J. P., Bui, T., Dean-Day, J. M., Thompson, C. R., Peischl, J., Ryerson, T. B., Bourgeois, I., Daube, B. C., Commane, R., and Wofsy, S. C.: Ambient aerosol properties in the remote atmosphere from global-scale in situ measurements, Atmos. Chem. Phys., 21, 15 023–15 063, https://doi.org/10.5194/acp-21-15023-2021, 2021.

Burkhardt, U., Bock, L., and Bier, A.: Mitigating the contrail cirrus climate impact by reducing aircraft soot number emissions, npj Climate and Atmospheric Science, 1, 37, https://doi.org/10.1038/s41612-018-0046-4, 2018.

Chen, H., Liu, B., Liu, R., Weng, Q., Zhang, T., and Pei, P.: Optimal interval of air stoichiometry under different operating parameters and electrical load conditions of proton exchange membrane fuel cell, Energy Conversion and Management, 205, 112 398, https://doi.org/https://doi.org/10.1016/j.enconman.2019.112398, 2020.

Commission, E., for Mobility, D.-G., Transport, for Research, D.-G., and Innovation: Flightpath 2050 – Europe's vision for aviation – Maintaining global leadership and serving society's needs, Publications Office, https://doi.org/doi/10.2777/50266, 2011.

https://doi.org/10.5194/jecats-2026-16
Preprint. Discussion started: 25 August 2026

Dischl, R., Sauer, D., Voigt, C., Harlaß, T., Sakellariou, F., Märkl, R., Schumann, U., Scheibe, M., Kaufmann, S., Roiger, A., Dörnbrack, A., Renard, C., Gauthier, M., Swann, P., Madden, P., Luff, D., Johnson, M., Ahrens, D., Sallinen, R., Schripp, T., Eckel, G., Bauder, U., and Le Clercq, P.: Measurements of particle emissions of an A350-941 burning 100 % sustainable aviation fuels in cruise, Atmos. Chem. Phys., 24, 11 255–11 273, https://doi.org/10.5194/acp-24-11255-2024, 2024.

Frey, A. C., Bosak, D., Madrid, E., Stonham, J., Sangan, C. M., and Pountney, O. J.: Thermal management in high temperature proton exchange membrane fuel cells for aircraft propulsion systems, Progress in Aerospace Sciences, https://doi.org/10.1016/j.paerosci.2024.101052, 2025.

Fuchs, N. and Sutugin, A. G.: Highly dispersed aerosols, Topics in Current Aerosol Research, 2, 1–60, 1971.

Fuel Cells and Hydrogen 2 Joint Undertaking: Hydrogen-powered aviation – A fact-based study of hydrogen technology, economics, and climate impact by 2050, Publications Office, https://doi.org/doi/10.2843/471510, 2020.

Gierens, K.: Theory of Contrail Formation for Fuel Cells, Aerospace, 8, https://doi.org/10.3390/aerospace8060164, 2021.

Hillenbrand, D.: Box model simulation results and plotting script for study on HDN effect in fuel cell propelled aircraft plumes, https://doi.org/10.5281/zenodo.21916005, 2026.

Hillenbrand, D. and Unterstrasser, S.: Contrail formation: generalised theory and a mitigation proposition for fuel-cell-propelled aircraft, The Aeronautical Journal, pp. 1–26, https://doi.org/10.1017/aer.2026.10185, 2026.

Hofer, S., Gierens, K., and Rohs, S.: Contrail formation and persistence conditions for alternative fuels, Meteorol. Z., 33, 43–49, https://doi.org/10.1127/metz/2024/1178, 2024.

HY4, 2016: First flight HY4, https://www.dlr.de/en/latest/news/2016/20160929_zero-emission-air-transport-first-flight-of-four-seat-passenger-aircraft-hy4_19469, 2016.

IAPWS, 1995: Properties of water, https://iapws.org/documents/release/Surf-H2O, 1995.

Jansen, J. and Heymsfield, A. J.: Microphysics of Aerodynamic Contrail Formation Processes, J. Atmos. Sci., 72, 3293–3308, https://doi.org/10.1175/JAS-D-14-0362.1, 2015.

Kantrowitz, A.: Nucleation in Very Rapid Vapor Expansions, The Journal of Chemical Physics, 19, https://doi.org/10.1063/1.1748482, 1951.

Kärcher, B.: A trajectory box model for aircraft exhaust plumes, J. Geophys. Res., 100, 18 835–18 844, 1995.

Kärcher, B., Burkhardt, U., Bier, A., Bock, L., and Ford, I. J.: The microphysical pathway to contrail formation, J. Geophys. Res., 120, 7893–7927, https://doi.org/10.1002/2015JD023491, 2015.

Kaufmann, S., Dischl, R., and Voigt, C.: Regional and seasonal impact of hydrogen propulsion systems on potential contrail cirrus cover, Atmos. Environ., 24, 100 298, https://doi.org/10.1016/j.aeaoa.2024.100298, 2024.

Kazula, S., de Graaf, S., and Enghardt, L.: Review of fuel cell technologies and evaluation of their potential and challenges for electrified propulsion systems in commercial aviation, Journal of the Global Power and Propulsion Society, 7, 43–57, https://doi.org/10.33737/jgpps/158036, 2023.

Kleine, J., Voigt, C., Sauer, D., Schlager, H., Scheibe, M., Jurkat-Witschas, T., Kaufmann, S., K/"archer, B., and Anderson, B. E.: In Situ Observations of Ice Particle Losses in a Young Persistent Contrail, Geophys. Res. Lett., 45, 13 553–13 561, https://doi.org/10.1029/2018GL079390, 2018.

Lee, D. S., Fahey, D. W., Skowron, A., Allen, M. R., Burkhardt, U., Chen, Q., Doherty, S. J., Freeman, S., Forster, P. M., Fuglestvedt, J., Gettelman, A., De León, R. R., Lim, L. L., Lund, M. T., Millar, R. J., Owen, B., Penner, J. E., Pitari, G., Prather, M. J., Sausen, R., and Wilcox, L. J.: The contribution of global aviation to anthropogenic climate forcing for 2000 to 2018, Atmos. Environ., 244, 117 834, https://doi.org/10.1016/j.atmosenv.2020.117834, 2021.

https://doi.org/10.5194/jecats-2026-16
Preprint. Discussion started: 25 August 2026

Lee, D. S., Allen, M. R., Cumpsty, N., Owen, B., Shine, K. P., and Skowron, A.: Uncertainties in mitigating aviation non-CO2 emissions for climate and air quality using hydrocarbon fuels, Environ. Sci.: Atmos., 3, 1693–1740, https://doi.org/10.1039/D3EA00091E, 2023.

Lewellen, D. C.: A Large-Eddy Simulation Study of Contrail Ice Number Formation, J. Atmos. Sci., 77, 2585–2604, https://doi.org/10.1175/JAS-D-19-0322.1, 2020.

Lottermoser, A. and Unterstrasser, S.: Towards intermediate complexity modelling of contrail formation: the new dynamical framework RadMod, Aeronaut. J., 129, 351–379, https://doi.org/10.1017/aer.2024.130, 2024.

Lottermoser, A. and Unterstrasser, S.: Modeling the Impact of Alternative Fuels and Hydrogen Propulsion on Contrail-Cirrus: A Parameter Study, J. Geophys. Res., 131, e2025JD044 604, https://doi.org/10.1029/2025JD044604, 2026.

Märkl, R. S., Voigt, C., Sauer, D., Dischl, R. K., Kaufmann, S., Harlaß, T., Hahn, V., Roiger, A., Weiß-Rehm, C., Burkhardt, U., Schumann, U., Marsing, A., Scheibe, M., Dörnbrack, A., Renard, C., Gauthier, M., Swann, P., Madden, P., Luff, D., Sallinen, R., Schripp, T., and Le Clercq, P.: Powering aircraft with 100 % sustainable aviation fuel reduces ice crystals in contrails, Atmos. Chem. Phys., 24, 3813–3837, https://doi.org/10.5194/acp-24-3813-2024, 2024.

Neumann, G., Marsing, A., Harlass, T., Sauer, D., Braun, S., Pühl, M., Heckl, C., Stock, P., De La Torre Castro, E., Hahn, V., Roiger, A., Voigt, C., Unterstraßer, S., Cammas, J., Renard, C., Vasenden, R., Vasenden, A., and Jurkat-Witschas, T.: In-flight emission measurements with an autonomous payload behind a turboprop aircraft, Atmos. Meas. Tech., 18, 6795–6816, https://doi.org/10.5194/amt-18-6795-2025, 2025.

Ocko, I. B. and Hamburg, S. P.: Climate consequences of hydrogen emissions, Atmos. Chem. Phys., 22, 9349–9368, https://doi.org/10.5194/acp-22-9349-2022, 2022.

Petzold, A., Fiebig, M., Keil, A., Leiterer, U., Schröder, F., Stifter, A., Wendisch, M., and Wendling, P.: Vertical variability of aerosol properties observed at a continental site during the Lindenberg Aerosol Characterization Experiment (LACE 98), J. Geophys. Res., 107, 8128, https://doi.org/10.1029/2001JD001043, 2002.

Ponsonby, J., King, L., Murray, B. J., and Stettler, M. E. J.: Jet aircraft lubrication oil droplets as contrail ice-forming particles, Atmos. Chem. Phys., 24, 2045–2058, https://doi.org/10.5194/acp-24-2045-2024, 2024.

Pope, S. B.: Turbulent Flows, Cambridge University Press, https://doi.org/10.1017/CBO9780511840531, 2000.

Richardson, E. S.: Contrail Formation Criterion for Assessment of Alternative Propulsion Technologies, Journal of Propulsion and Power, 41, 264–276, https://doi.org/10.2514/1.B39430, 2025.

Schumann, U.: On conditions for contrail formation from aircraft exhausts, Meteorol. Z., 5, 4–23, https://doi.org/10.1127/metz/5/1996/4, 1996.

Seinfeld, J. and Pandis, S.: Atmospheric Chemistry and Physics: From Air Pollution to Climate Change, WILEY INTERSCIENCE, 1998.

Sölch, I. and Kärcher, B.: A large-eddy model for cirrus clouds with explicit aerosol and ice microphysics and Lagrangian ice particle tracking, Q. J. R. Meteorol. Soc., 136, 2074–2093, https://doi.org/10.1002/qj.689, 2010.

Sölch, I. and Kärcher, B.: Process-oriented large-eddy simulations of a midlatitude cirrus cloud system based on observations, Q. J. R. Meteorol. Soc., 137, 374–393, 2011.

Starzmann, J., Hughes, F. R., Schuster, S., White, A. J., Halama, J., Hric, V., Kolovratník, M., Lee, H., Sova, L., Št'astný, M., Grübel, M., Schatz, M., Vogt, D. M., Patel, Y., Patel, G., Turunen-Saaresti, T., Gribin, V., Tishchenko, V., Gavrilov, I., Kim, C., Baek, J., Wu, X., Yang, J., Dykas, S., Wróblewski, W., Yamamoto, S., Feng, Z., and Li, L.: Results of the International Wet Steam Modeling Project, Proceedings of the Institution of Mechanical Engineers, Part A: Journal of Power and Energy, 232, 550–570, https://doi.org/10.1177/0957650918758779, 2018.

https://doi.org/10.5194/jecats-2026-16
Preprint. Discussion started: 25 August 2026

Unterstrasser, S.: Large eddy simulation study of contrail microphysics and geometry during the vortex phase and consequences on contrail-to-cirrus transition, J. Geophys. Res., 119, 7537–7555, https://doi.org/10.1002/2013JD021418, 2014.

Unterstrasser, S. and Gierens, K.: Numerical simulations of contrail-to-cirrus transition - Part 2: Impact of initial ice crystal number, radiation, stratification, secondary nucleation and layer depth, Atmos. Chem. Phys., 10, 2037–2051, https://doi.org/10.5194/acp-10-2037-2010, 2010.

Unterstrasser, S., Gierens, K., Sölch, I., and Lainer, M.: Numerical simulations of homogeneously nucleated natural cirrus and contrail-cirrus. Part 1: How different are they?, Meteorol. Z., 26, 621–642, https://doi.org/10.1127/metz/2016/0777, 2017.

Vancassel, X., Mirabel, P., and Garnier, F.: Numerical simulation of aerosols in an aircraft wake using a 3D LES solver and a detailed microphysical model, Int. J. Sustainable Aviation, 1, 139–159, https://doi.org/10.1504/IJSA.2014.065480, 2014.

Voigt, C., Kleine, J., Sauer, D., Moore, R. H., Bräuer, T., Le Clercq, P., Kaufmann, S., Scheibe, M., Jurkat-Witschas, T., Aigner, M., Bauder, U., Boose, Y., Borrmann, S., Crosbie, E., Diskin, G. S., DiGangi, J., Hahn, V., Heckl, C., Huber, F., Nowak, J. B., Rapp, M., Rauch, B., Robinson, C., Schripp, T., Shook, M., Winstead, E., Ziemba, L., Schlager, H., and Anderson, B. E.: Cleaner burning aviation fuels can reduce contrail cloudiness, Commun. Earth Environ., 2, 114, https://doi.org/10.1038/s43247-021-00174-y, 2021.

Voigt, C., Märkl, R., Sauer, D., Dischl, R., Renard, C., Seeliger, K., Yu, F., Kaufmann, S., Bräuer, T., Jurkat-Witschas, T., Le Chenadec, G., Moreau, J., Requena-Esteban, E., Bonne, N., Vals, M., Roche, A., Zelina, J., Dörnbrack, A., Eirenschmalz, L., Heckl, C., Horst, E., Lichtenstern, M., Marsing, A., Neumann, G., Roiger, A., Scheibe, M., Stock, P., Giez, A., Eckel, G., and Le Clercq, P.: Substantial aircraft contrail formation at low soot emission levels, Nature, 652, 112–118, https://doi.org/10.1038/s41586-026-10286-0, 2026.

Wilhelm, L., Gierens, K., and Rohs, S.: Weather Variability Induced Uncertainty of Contrail Radiative Forcing, Aerospace, 8, https://doi.org/10.3390/aerospace8110332, 2021.

Wittmann, T., Lück, S., Bode, C., and Friedrichs, J.: Modelling the Condensation Phenomena within the Radial Turbine of a Fuel Cell Turbocharger, International Journal of Turbomachinery, Propulsion and Power, 6, https://doi.org/10.3390/ijtpp6030023, 2021.

Wölk, J. and Strey, R.: Homogeneous Nucleation of H2O and D2O in Comparison: The Isotope Effect, The Journal of Physical Chemistry B, 105, 11 683–11 701, https://doi.org/10.1021/jp0115805, 2001.

Wölk, J., Strey, R., Heath, C. H., and Wyslouzil, B. E.: Empirical function for homogeneous water nucleation rates, The Journal of Chemical Physics, 117, 4954–4960, https://doi.org/10.1063/1.1498465, 2002.

Yin, F., Grewe, V., and Gierens, K.: Impact of Hybrid-Electric Aircraft on Contrail Coverage, Aerospace, 7, https://doi.org/10.3390/aerospace7100147, 2020.

Yu, F., Kärcher, B., and Anderson, B. E.: Revisiting Contrail Ice Formation: Impact of Primary Soot Particle Sizes and Contribution of Volatile Particles, Environ. Sci. Technol., 58, 17 650–17 660, https://doi.org/10.1021/acs.est.4c04340, 2024.

Zhang, Y., Hu, Z., Xu, L., Liu, H., Ye, K., Li, J., and Ouyang, M.: Fuel cell system for aviation applications: Modeling, parameter sensitivity, and control, Energy Conversion and Management, 312, 118 555, https://doi.org/https://doi.org/10.1016/j.enconman.2024.118555, 2024.

Zink, J. and Unterstrasser, S.: Contrail formation for aircraft with hydrogen combustion - Part 2: Engine-related aspects, EGUsphere, pp. 1–34, https://doi.org/10.5194/egusphere-2025-3708, 2025.

Zink, J., Unterstrasser, S., and Burkhardt, U.: Contrail formation for aircraft with hydrogen combustion - Part 1: A systematic microphysical investigation, EGUsphere, pp. 1–27, https://doi.org/10.5194/egusphere-2025-3704, 2025a.

Zink, J., Unterstrasser, S., and Jurkat-Witschas, T.: On the Potential Role of Lubrication Oil Particles in Contrail Formation for Kerosene and Hydrogen Combustion, J. Geophys. Res., 130, https://doi.org/10.1029/2025jd043487, 2025b.